Satellite-Based Characterization of Convection and Impacts from the Catastrophic 10 August 2020 Midwest U.S. Derecho

Jordan R. Bell,[a] Kristopher M. Bedka,[b] Christopher J. Schultz,[a] Andrew L. Molthan [a], Sarah D. Bang,[a] Justin Glisan,[c] Trent Ford,[d] W. Scott Lincoln,[e] Lori A. Schultz,[a] Alexander M. Melancon, [f] Emily F. Wisinski,[f] Kyle Itterly,[g] Cameron R. Homeyer,[i] Daniel J. Cecil,[a] Craig Cogil,[j] Rodney Donavon,[j] Eric Lenning,[e] Ray Wolf [k]

[a] Earth Science Branch, NASA/Marshall Space Flight Center, Huntsville, Alabama

[b] NASA Langley Research Center, Hampton, Virginia

[c] Iowa Department of Agriculture and Land Stewardship, Des Moines, Iowa

[d] Illinois State Water Survey, University of Illinois, Champaign, Illinois

e NOAA/NWS Weather Forecast Office, Chicago, Illinois

[f] Department of Atmospheric Science, University of Alabama in Huntsville, Huntsville, Alabama

[g] Science Systems & Applications, Inc., Hampton, Virginia

[i] School of Meteorology, University of Oklahoma, Norman, Oklahoma

j NOAA/NWS Weather Forecast Office, Des Moines, Iowa

k NOAA/NWS Weather Forecast Office, Davenport, Iowa

Corresponding author: Jordan R Bell, Earth Science Branch, NASA/Marshall Space Flight Center, 320 Sparkman Drive, Huntsville, Alabama, 35805

Email: jordan.r.bell@nasa.gov

ABSTRACT (250 WORDS)

The catastrophic derecho that occurred on 10 August 2020 across the Midwest United States caused billions of dollars of damage to both urban and rural infrastructure as well as agricultural crops, most notably across the state of Iowa. This paper documents the complex evolution of the derecho through the use of low-Earth orbit passive-microwave imager and GOES-16 satellite-derived products complemented by products derived from NEXRAD weather radar observations. Additional satellite sensors including optical imagers and synthetic aperture radar (SAR) were used to observe impacts to the power grid and agriculture in Iowa. SAR improved the identification and quantification of damaged corn and soybeans, as compared to true-color composites and Normalized Difference Vegetation Index (NDVI). A statistical approach to identify damaged corn and soybean crops from SAR was created with estimates of 1.97 million acres of damaged corn and 1.40 million acres of damaged soybeans in the state of Iowa. The damage estimates generated by this study were comparable to estimates produced by others after the derecho, including two commercial agricultural companies.

CAPSULE (BAMS ONLY—20 TO 30 WORDS)

The evolution and impacts of the historic 10 August 2020 Midwest derecho are analyzed using a diverse array of satellite sensors emphasizing collaborations within the NASA Applied Sciences Disasters Program.

-----ARTICLE START------

The severe thunderstorm and damaging wind event that spanned the upper Midwest U.S. on 10 August 2020 was the costliest thunderstorm event in U.S. history to date (Schwartz 2020). On this day, a derecho (Johns and Hirt, 1987; Corfidi et al. 2016) traversed the central United States and caused catastrophic damage to both urban and rural areas. Damage was especially pronounced across the state of Iowa where 59 counties were identified to have experienced crop and structural damage; 36 were extensive (NASS 2020). Wind gusts along the path were estimated up to 63 m-s-1 (140 mph) by using data from weather stations, damage reports, and storms surveys from multiple National Weather Service (NWS) that were impacted by the derecho (Figure 1). The Iowa Department of Natural Resources estimated that nearly 25% of the state's forests were lost (Beeman 2020), and the City of Cedar Rapids indicated that nearly 23,000 trees were damaged and required replacement (Jordan 2020). Downed trees and power lines interrupted power for 16 days around Cedar Rapids, further impacting the second largest city in the state (Steppe 2020). Winds from the derecho toppled grain storage bins and displaced them up to 5 km downwind, evidenced by thin linear tracks through the corn fields (Figure 2a). In 2019, Iowa and Illinois were at the top of state cash receipts for corn and soybeans (ERS 2021). The derecho damaged millions of acres of near-mature corn (Figure 2b), soybean (Figure 2c), and other crops in these two states with financial losses estimated from $6.8 (Munich RE 2021) to $11 B (NOAA NCEI, 2021). NWS Weather Forecast Offices surveyed 22 post-event tornadoes in the following derecho impacted County Warning Areas of Des Moines (4), Quad Cities (2), Chicago (11), Milwaukee/Sullivan (2), and Northern Indiana (3). Associated hail sizes up to 5 cm (~2 in.) in diameter were also reported near Breda, Iowa and in north central Illinois.

The 10 August 2020 derecho represents an extreme case of severe weather experienced in the Midwestern United States. Severe weather phenomena exhibit distinct signatures in spaceborne remote sensing datasets, showing characteristic structures in cloud-tops, in-cloud ice microphysics, electrical characteristics of the lightning, and surface damage in the storm's wake. In this paper, we present an overview of the 10 August 2020 derecho from multiple satellite-based remote sensing platforms in Low-Earth (LEO) and Geostationary (GEO) orbits. From these datasets, we will: 1) observe the derecho and varying stages of convective intensity by analyzing overshooting tops present in GOES-16 Advanced Baseline Imager (ABI) infrared brightness temperature (BT) and corresponding Geostationary Lightning Mapper (GLM) lightning rates, 2) infer presence of large hail through passive microwave brightness temperature depressions and confirm signatures using NEXRAD, 3) utilize data from optical remote sensing instruments, such as NASA MODIS, Suomi-NPP VIIRS, and ESA's Sentinel-2 Multispectral Instrument (MSI) to evaluate the impacts to the land surface, and 4) demonstrate a technique applying ESA Sentinel-1 synthetic aperture radar (SAR) and local anomalies to map and quantify agricultural losses in Iowa and Illinois. Collaborations with regional stakeholders including the NWS and the state climatologists for Iowa and Illinois demonstrate that signatures observed from these platforms are corroborated by other severe weather observations and both industry and governmental estimates of storm damage. We then compare these estimates against other available post-event assessments from the literature.

1. Derecho Evolution Depicted by Satellite and Radar Remote Sensing

a. Dataset Descriptions

Convection across the region of study was observed by the GOES-16 Advanced Baseline Imager (ABI, Schmit et al. 2017) instrument at five-minute intervals within the CONUS Domain Sector and at one-minute intervals within two Mesoscale Domain Sectors. The CONUS domain captures convective initiation and initial upscale growth, and the Mesoscale Domains capture the continued evolution of the derecho across Iowa, Illinois, and Indiana.

GOES-16 ABI data were resampled to a fixed grid with spacing of 56 pixels per degree which approximates to the 2 km ABI pixel spacing at nadir (Khlopenkov et al. 2021). We take the difference at each satellite pixel between the 10.3 µm infrared (IR) brightness temperature (BT) and the tropopause temperature calculated from Modern Era Retrospective analysis for Research and Applications, Version 2 reanalysis (MERRA-2; Gelaro et al. 2017). This difference normalizes cloud top temperatures relative to their ambient environment and identifies cloud top penetration into the lower stratosphere (Figure 3d). The hourly MERRA-2 tropopause temperature is spatially smoothed and interpolated temporally to 1-minute intervals and spatially to the 2 km ABI grid. The GOES-16 products are corrected for parallax error using cloud-top height derived from matching 10.3 µm IR temperature with the MERRA-2 sounding for temperatures warmer than the tropopause, and by employing the method of Griffin et al. (2016) for overshooting cloud top (OT) height assignment using a lapse rate of 6 K/km as OTs continue to cool as they ascend into the lower stratosphere. We refer to the difference between GOES-16 IR cloud top and the MERRA-2 tropopause temperatures as ∆Trop-IR, where positive values indicate cloud tops colder than the tropopause. GLM Flash Extent Density (FED) is aggregated at one-minute intervals using data from two-minute segments at the native GOES-16 ABI IR resolution, which is then resampled to the same 2-km grid (Figure 3e).

Level II volumetric radar data from Weather Surveillance Radar - 1988, Doppler (WSR-88D, Crum and Alberty 1993) sensors within the NEXRAD network were retrieved from the National Centers for Environmental Information (NCEI). All NEXRAD observations were obtained at a range resolution of 250 m, an azimuthal resolution of 0.5 degrees for the lowest 3-4 elevations and 1.0 degree otherwise, and typically at 14 elevations per volume scan. The data were processed using a modified version of the four dimensional (4-D) space-time merging methods known as Gridded NEXRAD WSR-88D Radar (GridRad; Homeyer and

Bowman 2017 and references therein), providing a wealth of radar observations at ~2-km horizontal resolution, 0.5 to 1-km vertical resolution, and 5-minute temporal resolution. GridRad products analyzed in this study include column-maximum radar reflectivity at horizontal polarization (Z_H, commonly referred to as "composite reflectivity," Figure 3a), Z_H = 20 dBZ tropopause-relative echo top height (Figure 3b), and hail differential reflectivity (HDR; Aydin et al. 1986; Depue et al. 2007, Figure 3c), which depends on Z_H and differential radar reflectivity (Z_{DR}). A 20-dBZ echo top threshold was selected to minimize noise and spatial incoherence that can occur with lower reflectivity thresholds. Depue et al. (2007) found that HDR exceeding 20 dB is correlated with severe hail (>19 mm diameter). Radial velocity is not included in the GridRad composite because it is a relative measurement to each fixed radar location and thus unique to the viewing geometry. Examination of velocity-based fields that are independent of viewing geometry (e.g., radial and azimuthal derivatives of radial velocity) can be merged into GridRad and are not included here due to: 1) the relatively large distance between Cedar Rapids and the Davenport and Des Moines NEXRAD sites that limit the quality of observations below 2 km, and 2) the wind direction along the squall line was not uniformly oriented along a radial toward either of the radar sites which would bias the velocity estimates.

The most extreme values from 2 km gridded GOES-16 1-minute imagery and GridRad 5-minute NEXRAD composites from 0800 to 2200 UTC are plotted in Figures 3a-e to demonstrate how satellite and radar remote sensing instruments depicted the evolution of the derecho. The column-maximum Z_H data are plotted hourly to facilitate interpretation of the precipitation spatial structure and the squall line "bow echo" and "comma head" shapes common to derechos (Przybylinski 1995).

Several LEO satellites carry passive-microwave radiometers that measure upwelling microwave radiation emitted from Earth's surface. If a cloud contains ice particles, the ice will scatter away the upwelling radiation, resulting in a lower (or "depressed") microwave BT relative to the scene around it (Vivekanandan et al. 1991). Different microwave frequencies are sensitive to scattering by different-sized particles. For example, a high frequency (e.g, 89-GHz or 3.4 mm) channel can be depressed by ice particles with diameters of a few millimeters (small graupel or other precipitating particles) that are comparable in size to the wavelength of the radiation. In contrast, low frequencies such as 37-GHz (8 mm) are mainly insensitive to the smaller particles (Mroz et al. 2017) but will be scattered efficiently by larger particles like graupel and hail. Leveraging the BT depressions and the channels in which they are expressed can provide some insight into the ice microphysics in the cloud. Spencer et al. (1987) first noted a relationship between the likelihood of severe weather with decreasing BT. The advancement of passive-microwave radiometry, additional channels, and finer spatial resolution have led to the advent of numerous severe weather detection and retrieval algorithms to exploit this relationship, especially for hail (Cecil 2009, Cecil and Blankenship 2012, Ferraro et al. 2015, Ni et al. 2017, Mroz et al. 2017, Laviola et al. 2020a; 2020b, Bang and Cecil 2019; 2021). Two passive-microwave radiometers: the DMSP F-17 Special Sensor Microwave Imager/Sounder (SSMIS) and Global Change Observation Mission 1st - Water (GCOM-WI) Advanced Microwave Scanning Radiometer (AMSR2) instruments observed the derecho and their imagery will be discussed below.

b. Analysis of Derecho Evolution

The derecho began with convective cells that formed west of Yankton, South Dakota and later expanded in area and moved southeastward into northeastern Nebraska. GOES-16 and GridRad metrics of very deep and intense convection (column-maximum Z_H > 50 dBZ, GLM FED > 22.5 flashes 2 min^{-1}, and ΔTrop-IR > 10 K) were all present at this early stage of the storm lifecycle (Figs. 3a, d-e). The DMSP F-17 SSMIS instrument observed the storm system at 1342 UTC. Imagery from the SSMIS 37-GHz and 91-GHz BTs and the corresponding GridRad column-maximum Z_H are shown in Figure 4a-c. Both channels exhibit depressed BTs over the deep convection, but, not in the same location. As discussed in the previous section, the two channels are primarily sensitive to different size particles and column integrated ice concentration. The 37-GHz BT (sensitive to scattering by larger ice and graupel particles) is correspondingly minimized along the Nebraska/Iowa border, co-located with the GOES-16 and GridRad storm intensity metrics listed above.

The storm system continued to intensify as it moved across western Iowa, where the axis of the highest echo tops moved south of Sioux City and became oriented into several distinct streaks (see dashed lines in Figure 3a-b). Cells with overshooting tops were correlated with frequent observations of ΔTrop-IR > 10 K, GLM FED > 10 flashes/2 min, and HDR > 27.5 dBZ. Hail up to 4 cm was reported in the northernmost overshooting cell, along with winds of up to 27 m s^{-1} (60 mph) in Breda, Iowa (Figure 1). This was one of the few hail reports from this event, even though HDR indicated the presence of hail aloft throughout the state. We speculate that the combination of wind and hail could have shredded already drought-damaged corn and soybeans, damage that is depicted in photographs from 11 August 2020 (Figure 5a-b). A localized hail scar was also evident in ESA Sentinel-2 Multispectral Instrument (MSI) imagery northeast of Breda where the photos were taken (Figure 5c). The nature of the crop damage and Sentinel-2 imagery here is notably different than that shown in Figure 2 where wind damage occurred exclusively. Between 1445 and 1545 UTC, peak measured winds in the line increased to 38 m s^{-1} (85 mph), and the number of damage reports to trees, buildings, and vehicles increased as the bow echo became more pronounced and echo tops remained above the tropopause. After 1545 UTC, the bow echo approached Des Moines with the comma head located near Ames, Iowa (see arrow, Figure 3a). Another wind gust measured at 38 m s-1 occurred at Elkhart, Iowa at 1610 UTC just north of Des Moines, generated by an intense cell with overshooting echo tops and high ΔTrop-IR, HDR, and GLM FED values above 25 flashes/2 minutes.

Between 1630 and 1800 UTC the most extreme damage from the event was generated from Marshalltown through Cedar Rapids, Iowa. Four tornadoes were identified near Marshalltown between 1630 and 1645 UTC. The cells that generated the tornadoes did not stand out from other intense cells in the western half of Iowa from a GOES-16 and GridRad column-maximum Z_H perspective. Extreme winds between 53 and 58 m s^{-1} were estimated in Benton County to the west of and throughout Cedar Rapids. Wind gusts immediately south of the derecho comma head (grey arrows in Figure 3) and along the apex of the bow echo indicate an intense rear-inflow jet (Smull and Houze 1987). Two areas of overshooting echoes were present in this area, one extending from Marshalltown through Cedar Rapids at the bow apex and another just north of Cedar Rapids within the comma head. At 1746 UTC when the bow echo was moving through Cedar Rapids (Figure 6a), the coldest IR temperature (197 K) occurred just north and west of the city, while a plume of warmer IR temperatures was overhead (Figure 6b). The warm anomaly is associated with an above-anvil cirrus plume (Bedka et al. 2018) generated by the intense updraft west of the city. Another plume was generated by a cell that produced 2.5 cm hail in Cascade, Iowa, southwest of Dubuque. A small area of cold IR BT (< 203 K, white color in Figure 6) and column-maximum Z_H > 50 dBZ was present to the northwest of Iowa City indicating vigorous convection at the apex of the bow. In general, though, the IR BT pattern does not resemble the GridRad column-maximum Z_H bow echo shape, but the coldest BT did coincide with the highest echo tops, as would be expected.

The derecho continued to propagate eastward to the Quad Cities region bordering eastern Iowa and northwest Illinois from 1800 to 1900 UTC. Wind reports were oriented from Iowa City to the Davenport, Iowa region, along the edge of the 36 m s^{-1} (81 mph) peak wind gust swath analyzed by the NWS, where relatively weak ΔTrop-IR (0 to 5 K) and minimal lightning activity was observed. A 122-m tower that was rated to withstand winds up to 58 m s^{-1} was toppled near Clinton, Iowa, where the Clinton automated weather observing system recorded gusts over 27 m s^{-1} for nearly 45 minutes. This occurred within the apex of the bow that previously moved across Cedar Rapids, where echo tops above the tropopause had re-emerged (dashed line, Figure 3). At 1852 UTC (1352 CDT), the AMSR2 instrument observed the derecho on the Iowa-Illinois border, and the 37- and 89-GHz PCT, and GridRad Z_H is shown in Figure 4d-f. These two channels are comparable to those shown in Figure 4a-c from SSMIS, however, AMSR2 has much finer spatial resolution (SSMIS: 37 x 28 km, AMSR2: 12 x 7 km), and therefore ASMR2 imagery shows a much more pronounced contrast and significantly depressed BTs where high column-maximum Z_H indicates significant ice scattering is likely to occur. Though AMSR2 temperatures were low for the cell that impacted Clinton, Iowa (~145 K at 37 GHz), they were even lower (< 130 K) for a pair of supercell storms that developed northeast of the primary squall line in extreme southwest Wisconsin. One of these cells had previously generated severe winds and a tornado north of Dubuque, Iowa (see Figure 1) and another generated 5 cm hail near Freeport, Illinois, shortly after the AMSR2 observation. Echo tops above the tropopause, large ΔTrop-IR, and high HDR were present at the time of the Freeport large hail report, but with less lightning activity (5 flashes/2 mins).

As the derecho moved farther eastward, winds continued to produce widespread damage from southern Wisconsin through Illinois, and numerous tornadoes developed in northeastern Illinois. An axis of persistent overshooting echo tops extended from north of Dixon through Aurora and north of Kankakee which were collocated with a high concentration of wind damage reports and several tornadoes. Tornadoes occurring from west of Aurora to Chicago were generated by intense but small cells (< 10 km diameter) embedded within subtle bows in the squall line. Very narrow cores of ΔTrop-IR > 10 K and echo top above the tropopause were observed in northeast Illinois, but with much lower flash rates (< 5 flashes/2 mins) than areas to the north in southeastern Wisconsin along the comma head. Only one pulse in FED to 20 flashes/2 minutes was observed near Aurora, Illinois, around the time of the tornadoes that affected the south suburbs of Chicago. The derecho continued its path through central Illinois, northern Indiana, and southwest Michigan, where widespread wind damage and wind gusts up to 31 m s^{-1} continued and hail up to 2.5 cm was reported. Additional tornadoes occurred in northern Indiana that were rated as EF-1 on the Enhanced Fujita tornado damage scale (Texas Tech 2004). Wind damage continued across much of Indiana, Illinois, and Missouri through 0300 UTC. As the derecho entered Ohio and Kentucky, the system weakened considerably, and no additional reports were received.

The relationships between satellite-derived products and observed severe weather conditions were quite complicated for this event. The coldest IR BT, highest echo tops, highest HDR, and largest FED values were highly correlated near the comma head of the derecho (across western Iowa) and supercells ahead of the primary squall line (eastern Iowa into southern Wisconsin). This area corresponds to the axis of highest winds, power loss, and damage across Iowa. FED values were highest along the same axis as the comma head region of the derecho and were more muted within the bowing segment across northern Illinois as the derecho pushed eastward. Initially FED was correlated with echo top heights and large ΔTrop-IR as the mixed phase updrafts embedded within the squall line fluctuated and the line traversed across the domain; however, de-correlation between echo top height and FED occurred across northeast Illinois. This decorrelation is similar to other mesoscale convective systems studied in Carey et al. (2005), Makowski et al. (2013), and Schultz et al. (2015) as lightning initiation occurs in the convective line and propagates rearward into the stratiform region. As the derecho matured and elongated to the south after passing Des Moines, severe wind reports continued to occur near Iowa City and Davenport, yet IR temperature, FED, and echo tops were much weaker than areas to the north. Severe winds were driven by the presence of a cold pool behind the line and downdrafts not favorable for generation of intense lightning activity. The storm cells that generated catastrophic damage to Cedar Rapids did not look notably different in the satellite imagery from other time frames, such as when the line was across western Iowa, where extreme winds were not observed. The coldest GOES-16 IR cloud top temperatures and highest FED remained 10-20 km north of Cedar Rapids and displaced from the most extreme winds. Many automated nowcasting products and precipitation retrievals assume that the coldest IR BT and greatest lightning activity equate to the most extreme weather. The satellite observations of the 10 August derecho event highlight the challenges of using satellite cloud top information to infer weather conditions at the ground. In contrast, the SSMIS and AMSR2 data depicted areas of intense convection well, but the AMSR2, with its finer spatial resolution, was better able to distinguish individual intense cells at the single snapshot in time that this low-Earth-orbit based observation occurred.

2. Mapping Derecho Impacts using Passive Remote Sensing

a. Power Grid Impacts

Multiple utility companies experienced significant interruptions to the electrical grid as a result of the derecho. At the peak, an estimated 1.9 million customers across the derecho path were impacted with disruptions of service to approximately 585,000 customers in Iowa (PowerOutage 2021a). With multiple power companies servicing the area, (PowerOutage 2021b), satellite imagery can offer a qualitative assessment of where city lights may be missing from power outages. VIIRS includes a panchromatic Day/Night Band (DNB) that measures light over the spectral range of 0.5 µm - 0.9 µm, making it sensitive to a large dynamic range of low-light conditions. (Lee et al. 2006), enabling the daily monitoring of nighttime phenomena, which are mainly anthropogenic light sources.

The NASA Black Marble team produces a daily top-of-atmosphere (TOA), at-sensor nighttime radiance product called the VIIRS/NPP Daily Gridded Day Night Band which contains 26 science data products including the sensor radiance, cloud mask, and coincident VIIRS moderate-resolution infrared bands at a 15 arc-second (~460 m at equator) spatial resolution. All data products are processed within 3-5 hours after acquisition and are acquired through the Level-1 and Atmosphere Archive & Distribution System (LAADS) Distributed Active Archive Center (DAAC: Roman et al. 2018).

Using only the DNB radiance data, clouds at varying heights are hard to detect on low- or moonless nights, making the qualitative assessment of city lights difficult (Figure 7a). A simple-to-use false color composite assigns the DNB to the red and green channels and the longwave infrared (10.76 μm) to the blue channel, producing a product (DNB/IR) that highlights the presence of many optically thick clouds of varying altitudes. This resulting image shows observed city light in yellow, while clouds will vary in color from blue to yellow to white, depending on their height and the available illumination from the moon (Figure 7b). Other bands or false color composites (e.g, Nighttime Microphysics, NtMicro 2022) can help confirm the presence of low or thin clouds (e.g., cirrus, fog) that may also be present.

Using the DNB/IR false-color composite from 10 August 2020 (pre-derecho, Figure. 8a) and comparing it to 11 August 2020 (post-derecho, Figure 8b), the extent and impact to the electrical grid can be seen. Although there are some thin clouds present, the large difference in the amount of light observed by the sensor especially in areas of Cedar Rapids and Iowa City (orange circle), Davenport (yellow circle), and smaller cities to the east of Des Moines (white circle) depicts the widespread loss of light, likely due to a power outage. The DNB composites on 14 August (Figure 8c) and 26 August (Figure 8d) show increases in the amount of light as power was restored.

b. Land Surface Impacts

Satellite remote sensing has often been used to assess damage to the land surface from severe thunderstorms. Satellite imagery has been used in combination with ground surveys to confirm and map tornado tracks (Yuan et al. 2002, Jedlovec et al. 2006, Molthan et al. 2014, Molthan et al. 2020). Imagery has been used to observe and analyze hail damage swaths across agricultural areas in the Midwest (Molthan et al. 2013, Bell and Molthan 2016, Gallo et al. 2019, and Bell et al. 2020). Previous studies often leverage optical remote sensing instruments to assess the impacts to the land surface, by using commonly available red (0.65 µm) and near-infrared (0.85 µm) spectral bands. These bands are used in the Normalized Difference Vegetation Index (NDVI) calculations from MODIS which is frequently used. to map the status of vegetation greenness and health (Rouse et al. 1974, Tucker 1979).

In the immediate hours after the derecho moved through Iowa, numerous reports from officials (NWS, State, and local government) and social media (Facebook and Twitter) began relaying that acres of crops were flattened due to high winds (Figure 2b-c). Corn and soybeans, the two major crops in the region, were near peak maturity when the derecho occurred. The following afternoon (11 August 2020), the NASA Aqua MODIS sensor imaged most of the impacted areas in Iowa and western Illinois. When compared to pre-derecho true color imagery from 28 July 2020, several swaths of slight changes in the green shading appear compared to the rest of the region across central and eastern Iowa (Figure 9a-b). Moderate spatial resolution sensors like Landsat-8 Operational Land Imager (OLI) were able to capture several post-derecho passes where changes to the land surface color are distinguished in better detail (NASA EO 2020), but OLI observations are collected over a narrower swath and more infrequently than daily MODIS. MODIS NDVI imagery for the same pre- and post-derecho days showed small NDVI value decreases (0.1 to 0.2) where the change was inferred from true color composites (Figure 9c-d). Past efforts by Gallo et al. (2019) included establishing damage categories assessed through changes in NDVI. In this Iowa event, NDVI decreases of 0.1 to

0.2 (Figure 9e) would be characterized as “no damage,” however, post-derecho photography of the affected crops confirmed damage primarily from wind-based toppling of crops (Figure 2b-c), with minimal areas impacted by wind-driven hail (Figure 5 a-b), leaving a substantial amount of green vegetation material intact. Changes in NDVI were delayed until damaged crops either wilted and browned or were manually cleared, which could be several weeks post-derecho and obscured by changes in land surface color due to the transition into autumn.

3. Agricultural Damage Mapping Using Synthetic Aperture Radar

a. Qualitative SAR Analysis

SAR instruments provide another way to observe and analyze the land surface for impacts and changes from intense and severe thunderstorms regardless of overpass time and sky conditions. Unlike optical sensors that are passive, SAR instruments are active sensors, meaning they transmit and receive electromagnetic waves at certain frequencies and polarizations. They measure both the amplitude (intensity) and phase of the returned electromagnetic radiation to the sensor (Moreira 2013). The returned backscattered electromagnetic pulses are greatly impacted by the surface characteristics such as the canopy structure (size and shape), surface roughness, dielectric properties (soil type and moisture) and canopy water content (McNairn et al. 2009; Cable et al. 2014; Forkuor et al. 2014; Canisius et al. 2018). Incidence angle (Larrañaga and Álvarez-Mozos 2016), type of scattering (Freeman and Durden 1998; White et al. 2015), and polarization emitted and received (Haldar et al. 2012) can also influence the amplitude and phase of the received return pulse. The backscatter from targets is the combination of scattering from different sources, though one scattering mechanism is usually dominant (Jiao et al. 2011). The co-polarization [horizontal-horizontal (HH) or vertical-vertical (VV)] and cross-polarization [vertical-horizontal (VH) or horizontal-vertical (HV)] components of the emitted and received signal provide in-depth insight into the backscattering mechanisms of the targets being sampled (Karjalainen et al. 2008; Moreira et al. 2013; Li and Wang 2018).

SAR is an emerging tool for agricultural applications such as measuring soil moisture (Ulaby and Batlivala 1976, Kornelsen and Coulibaly 2013, Grelfeneder et al. 2018), classifying crops (McNairn et al. 2000, Whelen and Siqueira 2018), and monitoring crop conditions (Liu et al. 2013, McNairn et al. 2004, Wiseman et al. 2014). Vegetation and agricultural crops are more sensitive to the cross-polarization components (VH or HV) that capture the crop structure within the total canopy due to the volumetric scattering of the depolarized SAR signal in the dense canopy (Karjalainen et al. 2008; Li and Wang 2018). In early stages of crop growth, the soil surface dominates with a specular, surface scattering behavior (often, lower returns) whereas later in the growing season, the mature canopy provides an increase in volumetric scattering from complex plant shapes and structure, enhancing the utility of the cross-polarization channel from C-band instruments (Halder et al. 2012, Cable et al. 2014, McNairn et al. 2014). Shorter (longer) wavelength SAR instruments will see the surface scattering contribution decline (increase) with a growth and development in the canopy (Jiao et al. 2011, Cable et al. 2014).

Bell et al. (2020) demonstrated the value of ESA Sentinel-1 C-band SAR in mapping wind and hail damage to agriculture, observing an increase of 0.5 to 0.8 dB in co-polarized (VV) but a larger 1.2 to 2.5 dB change in cross-polarized (VH) amplitude when comparing damaged to undamaged regions. Hosseini et al. (2020) used Sentinel-1 data to provide damage estimates of corn and soybean crops impacted by the 10 August 2020 derecho event across Iowa. Observed backscatter values (dB) for a period of July and August 2019 were compared to observed backscatter values for July and August 2020 for 300 sites across 50 corn and 50 soybean fields in Iowa. After a thorough comparison and correlation of the co- and cross-polarizations for these sites, a change of 1.5 dB between pre- and post-derecho Sentinel-1 acquisitions was chosen to delineate damage across Iowa. This threshold fell between the range of 1.2 and 2.5 dB observed in the cross-polarization change in Bell et al. (2020). Hosseini et al. (2020) used this threshold to generate damage estimates of corn and soybean crops in impacted counties across Iowa and compared their damage estimates to the damage estimates of two private industry estimates, Indigo (Indigo 2020) and McKinsey and Company (McKinsey and Company 2020). The estimates generated by Hosseini et al. (2020) for damaged corn were 0.11 to 1.43 million acres (-5.5 to -71.9%) below the private companies' estimates and for soybeans 0.16 to 0.80 million acres below (-21.1% to -84.2%).

Active remote sensing of vegetation structure via SAR provides an improved visual depiction of crop damage, which motivates objective mapping. Post-derecho Sentinel-1 acquisitions occurred on 15 August over the western part of Iowa, 16 August for Eastern Iowa and Western Illinois, and 21 August for central Iowa. The Alaska Satellite Facility created their own false-color RGB Decomposition of Sentinel-1 Radiometric and Terrain Corrected (RTC) imagery that focuses on color interpretation based on the type of scattering (ASF 2021). Through careful assignment of scattering type signals to color intensities, undisturbed open water bodies appear blue, urban areas appear orange/brown, and areas of vegetation (e.g. agricultural crops, grasslands, and forest) appear green. Then, visual changes in coloration correspond to changes in the relative contributions of various scattering types.

A comparison of pre-derecho and post-derecho Sentinel-1 RGB Decomposition shows a visible change in green shading across Central Iowa that was compared visually to the damage swath depicted by MODIS, available storm reports, and other satellite-based metrics of storm severity (Figure 10a-b). The green component of the RGB decomposition is comprised solely of volumetric scattering, so an increase in volumetric scattering will change the green channel's contribution to the decomposition. Areas of brighter green intensities in the Sentinel-1 RGB Decomposition were generated by crops layering atop themselves in the damaged areas. This layering of damaged crops led to an increase in cross-polarized amplitude values which corresponds to an increase in volumetric scattering, and the increase in green coloration intensity. This is consistent with the increase in volumetric scattering found in late-season agricultural damage caused by severe thunderstorms in 2018 (Bell et al. 2020). The location of this swath aligns with numerous severe weather reports across the region (Figure 10c).

Multiple field tours, local and state-level reporting along with initial MODIS satellite images on 11 August (Figure 9b) helped provide robust initial guidance for various stakeholders (NWS, Iowa State Climatologist) to assess the damage in Iowa. Crop damage estimates became better detailed once the Sentinel-1 RGBs were provided to the National Weather Service and the Iowa State Climatologist (Figure 10b-c). Additional geo-tagged photos from surface and aerial surveys matched up well with the damage indicated by the Sentinel-1 RGB Decomposition.

The lack of significant crop damage outside of Rock Island, Whiteside, and Carroll Counties in Northwest Illinois was supported by the Sentinel-1 RGB Decompositions (Figure 10). Initial crop damage reports in Illinois were few in number, spatially isolated, and collected through individual conversations and social media despite the extent of severe winds across northern Illinois. The timely provision of this imagery was very helpful to (1) more accurately assess the spatial extent of crop damage in northern Illinois, (2) confirm isolated, on-the-ground reports of damage or lack of damage from University of Illinois Extension and producers, and (3) target damage assessment outreach from the Illinois State Climatologist Office.

a. Quantitative SAR Analysis

After sharing the Sentinel-1 RGB Decompositions with stakeholders in Iowa and Illinois, a post-event, in-depth, quantitative analysis was performed to provide estimate of damage sustained by the specific crops across Iowa and Illinois. This methodology was assessed against photography of damage and other available estimates derived from both optical and SAR remote sensing techniques (Hosseini et al. 2020, Indigo 2020, and McKinsey and Company 2020). The methodology in Bell et al. (2020) was modified with statistical and image processing techniques to identify damaged corn and soybeans left behind in wake of the derecho.

Starting with Sentinel-1 VH amplitude data processed by ASF (Hogenson 2016), anomalies between the "damaged" and "non damaged" corn and soybean pixels were calculated. Pixels were identified as corn or soybeans using the 2020 Crop Data Layer product (Boryan et al. 2011). Bell et al. (2020) and previous studies (Gallo et al. 2012, Molthan et al. 2013, Bell and Molthan 2016, Gallo et al. 2019) used derived weather radar reflectivity or derived estimates of maximum hail size and vegetation indices to compare areas impacted by damaging winds and large hail to non-impacted areas. Due to the lack of derived hail signatures in the radar data and the areal extent of the wind damage, this study utilized a threshold (3 K) from the GOES-16 ΔTrop-IR product to compare perceived "damaged" and "non-damaged background" corn and soybean crops. A GOES-16 ΔTrop-IR threshold of 3 K indicates storm tops just above the tropopause and provides a delineation between regions potentially damaged from strong convection from areas impacted by weaker convection. Use of this IR-based proxy promotes future extension of this methodology to remote or data-sparse regions without extensive weather radar coverage.

Corn and soybean Sentinel-1 VH amplitude values across Iowa and western Illinois were considered a part of the "non-damaged background" if there were at least 10 km outside the 3 K ΔTrop-IR boundary (Figure 11). The mean of the "non-damaged background" (μ_{crop}), Sentinel-1 amplitude values were then used in calculating amplitude anomalies for the two crop types across Iowa and western Illinois:

$$anomaly = VH_{crop} - \mu_{crop}.$$

A noticeable area of higher anomaly values was present across a large portion of Iowa (Figure 11). Bell et al. (2020) demonstrated that damaged crops brighten in the VH relative to their background. Therefore, positive anomalies are representative of local brightening of varying magnitudes relative to the non-damaged background.

Following the procedures as described in Bell and Molthan (2016) and Bell et al. (2020), we used the Sentinel-1 RGB Decomposition (VH brightening and change in RGB Decomposition) and GIS software to independently outline the extent of the visibly damaged areas by two researchers at the University of Alabama in Huntsville and one researcher with NASA's Marshall Space Flight Center. A final manually derived damage extent was retained where at least two of the three analyses intersected (Figure 12a).

The distribution of Sentinel-1 VH anomaly values of corn and soybean pixels inside the derived damaged extent were then compared to those outside the same boundary to compare the distribution between the two classes (Figure 12b). The near-normal distributions of VH amplitude anomaly values of the damaged and undamaged classes and separation of the two classes allowed for the Z-score to be calculated for the anomalous values of the Sentinel-1 VH amplitude. Individual pixels within the zone of potential damage were assigned a Z-score through calculation against the mean (μ_{crop}) and standard deviation (σ_{crop}) of the corn and soybean pixels in the "non-damaged background" derived from using the 3 K threshold in the GOES ΔTrop-IR for background pixels of the same crop type. The Z-score was calculated as follows:

$$Z = \frac{VH_{crop} - \mu_{crop}}{\sigma_{crop}}.$$

The Z-score shows how a corn or soybean pixel relates to the mean of the non-damaged background area. The histogram in Figure 12b shows two distinct classes of corn and soybean pixels: those within the manually derived damaged extent and those outside (Figure 12a). The anomaly values inside the damaged extent were positive because of the increase in volumetric scattering corresponds to higher VH amplitude values. The damaged (non-damaged) corn and soybean anomaly pixels had a mean amplitude value of 0.05 (0.01). This confirms that the cross-polarized values of the Sentinel-1 amplitude pixels were brighter in the damaged area than outside it. Figure 13a shows the very low Z-scores across Iowa and western Illinois in the “perceived non-damaged” areas, with a mean of 0.86 and a standard deviation of 0.69. Z-scores inside the derived damage extent area are higher and more variable, with a mean of 2.22 and a standard deviation of 1.32. Negative Z-score values were omitted since they were not indicative of brightening of the Sentinel-1 amplitude data, and therefore are unlikely to be damaged pixels (Figure 13a). The large area of positive anomalies aligns with a large number of the storm reports and NWS peak wind gusts in excess of 31 ms^{-1} (70 mph).

Varying Z-score thresholds were assessed for accuracy by converting the threshold to a binary mask for evaluation against the manually derived damage extent. Open-source image processing tools from Python and the scikit-image library (van der Walt et al. 2014) were utilized to remove identified damaged areas smaller than 2023 m^2 (0.5 acres) to reduce noise created through the despeckling of the Sentinel-1 RTCs. In order to evaluate the Z-score thresholds, Civil Air Patrol (CAP) imagery acquired within seven days of the derecho and available from the USGS Hazards Data Distribution System was used to identify random fields that had some degree of visible damage (Figure 13b-c) between Des Moines and Cedar Rapids, Iowa. The CAP imagery showed varying degrees of damage in the portions of the fields that were visible in the photographs. A total of 41 fields were identified, geolocated, and the areal extent of each field was determined (Figure 12a). Therefore, if a photographed portion of a field showed damage, the entire field was marked as damaged. The binary product for each Z-score threshold was evaluated to see how many of the 41 fields were identified as having at least one damaged pixel and what percentage of each field's total area was identified as damaged.

In evaluating the Z-score thresholds, selecting Z=1.2 identified 81.8% of the total area of the 41 validation fields as damaged while the Z=1.3 identified 79.5% of the total area. A detection rate of 80% of the total area amongst the 41 validation fields was selected to define a Z-score threshold when generating our damage estimates for impacted corn and soybean crops. 80% was deemed to be acceptable as this study did not have access to high resolution ground truth data for calibration and this was the first time that this methodology, the use of a derived satellite product instead of a ground-based radar product, had been attempted. Additionally, the 80% rate was determined to prevent potential overestimation by lower Z-scores and potential severe underestimation with higher Z-score thresholds. The Z-score values of 1.2 and 1.3 correspond to Sentinel-1 amplitude anomaly values of 0.086 and 0.089 respectively. Both of these Sentinel-1 anomaly values overlapped with the very far-right tail of non-damaged areas and were to the right of the mean amplitude anomaly value (0.049) of the damaged areas (Figure 12b). Positive anomaly values to the left of Z=1.2 and =1.3 may have been indicative of observed structural changes to the corn and soybean crops as a result of the derecho but may have also provided unrealistic damage estimates. Future work could seek to categorize potential damage severity, as demonstrated by Hosseini et al. (2020) and Gallo et al. (2019), albeit using NDVI data. Such an analysis would require extensive documentation of crop damage from the ground and sensors with higher spatial resolution. The 80% detection rate was determined to be sufficient for calibrating future algorithms and future work that improves detection with higher spatial resolution sensors. A final Z-score threshold value was chosen by taking the mean of these two Z-scores (1.25).

The chosen Z-score threshold of 1.25 (Sentinel-1 HV amplitude anomaly value of 0.0875) was then used to generate damage estimates of corn and soybean crops across Iowa and extreme western Illinois (Figure 14). The damage estimates generated for Iowa were compared to estimates provided by Hosseini et al. (2020), Indigo (2020) and McKinsey and Company (2020) in Table 1. We estimate 1.97 million acres of corn were damaged, 130 K (-6.2%) acres fewer than Indigo (2020). Our corn estimates are lower than McKinsey and Company (2020) estimates by about 510 K acres (-20.6 %). The estimates for damaged soybeans were nearly identical to the Indigo (2020) estimates, which exceed McKinsey and Company (2020) soybean damage estimates by 1.1 million acres (+351.6%). Our damage estimates compared with Hosseini et al. (2020) were 0.02 million few acres for corn (-1.0%) and 0.80 million acres more for soybeans (+133.3%). Variability within the damage estimates for each study can be attributed to various methodologies used by each study. All the studies utilized Sentinel-1 data from ESA. McKinsey and Company (2020) was the only estimate to document their methodology of using optical remote sensing data in conjunction with the SAR data.

All the estimates were then compared to county estimates provided by the United States Department of Agriculture (USDA) Risk Management Agency (RMA 2021, Table 1). USDA RMA damage estimates in the overlapping counties of the manually derived damage extent for their own damage categories of hail and wind/excess wind totaled 1.13 million acres, which is significantly below all other estimates. One contributing factor to the low RMA estimate is that several counties, especially on the western portion of the damage swath, were experiencing moderate to severe drought. According to the 9 August 2020 Vegetation Drought Response Index (NDMC 2020), areas of pre-drought stress extended from western parts of the damage areas eastward through portions of the central areas of the damage as well (Figure 15). We hypothesize that some crops impacted by the derecho were classified as drought damage and not hail or wind/excess wind damage. When factoring in the drought damage estimates for these counties, the USDA RMA estimate continued to be below all the estimates listed in this manuscript, by over 1 million total acres. Partially blown over crops, especially corn, could appear as damaged in the Sentinel-1 data, but not be sufficiently damaged enough to be included in the RMA estimates. The SAR-derived damage extent did cross the Mississippi River and stretch into Whiteside and Rock Island counties in Illinois. In those two counties, 26,217 acres of corn and 9,922 acres of soybean were identified as "damaged" using Sentinel-1 data. RMA damage estimates for these two counties were 21,060 acres of corn and 9,192 acres of soybeans (RMA 2021).

4. Conclusion

This manuscript highlights a diverse array of remote sensing observations that were used to analyze the catastrophic 10 August 2020 derecho over the Midwest United States. LEO passive-microwave imagers and 1-minute resolution GOES-16 products were used to track and characterize the evolution of the storm system. The coldest GOES-16 IR temperature, greatest FED, and highest GridRad echo tops and HDR (indicative of intense updrafts likely to have generated hail), were highly correlated across the parts of Iowa where the highest winds, power loss, and discernable hail damage in agricultural crops occurred. Several areas of de-correlation were noted where high winds were driven primarily by a cold pool from complex 4-D dynamics and precipitation within the derecho storm system. Our analyses demonstrate how GOES-16 and GridRad can be applied to study severe storm evolution and highlight opportunities for using satellite IR and lightning observations within cloud tops to infer severe weather conditions at the ground. A pair of passive-microwave radiometer observations from SSMIS and AMSR2 data can be used to infer regions with the most intense convection and scattering by large and/or high concentrations of ice particles. The spatial resolution of the passive-microwave sensors has a strong impact on the ability to resolve these smaller-scale convective phenomena.

Data and imagery captured by additional LEO satellites and photographs were used to assess the derecho's impacts to the land surface. Optical remote sensing instruments observed power outages, grain storage bins transported for large distances by extreme winds and scarring of the land surface believed to be caused by wind-driven hail. However, with the corn and soybean crops being near peak maturity when the derecho moved through, most of the damage outside of hail-producing cells consisted of the crops laying over with minimal change in vegetation color, limiting the ability of optical remote sensing instruments to discern damage. SAR provided more beneficial information for identifying damaged areas because it observes changes in crop structure and orientation as opposed to crop health and verdancy and is able to image the surface through cloud cover, unlike optical sensors. Using ESA Sentinel-1 data, we demonstrate a statistical approach to identify specific damaged pixels in the corn and soybean crops in post-derecho acquisitions. This approach was validated using aerial imagery captured in the days after the derecho. The damage estimates of the corn and soybeans generated from this technique were then compared to estimates from other sources, showing very good agreement.

This comprehensive overview shows the benefits of using satellite remote sensing for monitoring, tracking, and analyzing the impacts of intense thunderstorm events and could be beneficial for disaster response across the globe, especially in areas where ground observations and radar networks are sparse or nonexistent. Additionally, as future SAR missions launch, especially those (i.e. NISAR) with longer wavelengths than Sentinel-1, the authors anticipate being able to quantify changes in agricultural crops more accurately and with greater detail. Future work will focus on continuing analysis of satellite products for additional severe storm events in different regions where updraft intensity and land surface cover may differ, and documenting innovative ways that the diverse sensor data can be combined objectively to provide a holistic view of an event throughout its lifecycle.

Acknowledgments.

The authors thank the NASA Applied Sciences Disasters Program award which provided the funding for this work. The authors express a sincere thanks to colleagues at the Iowa and Illinois State Climatologist Offices, the National Weather Service Offices in Des Moines, Davenport, and Chicago, and the Alaska Satellite Facility. Finally, the authors express their gratitude to the reviewers who took time to provide input and comments to strengthen this manuscript.

Data Availability Statement.

NOAA Geostationary Operational Environmental Satellites (GOES) 16 Satellite data can be accessed the Registry of Open Data on AWS at the following link: https://registry.opendata.aws/noaa-goes/. Additional documentation on this data can be found at https://docs.opendata.aws/noaa-goes16/cics-readme.html. GOES-16 and GridRad derived products presented in this paper can be accessed at https://science-data.larc.nasa.gov/LaRC-SD-Publications/2021-07-07-001-KMB/.

Level 1C calibrated passive-microwave data are available for unlimited public download from the NASA Goddard Earth Sciences Data and Information Services Center (GES DISC) for DMSP F17 SSMIS at https://doi.org/10.5067/GPM/SSMIS/F17/1C/05 and GCOM-W1 AMSR2 at https://doi.org/10.5067/GPM/AMSR2/GCOMW1/1C/05

NPP Daily Gridded Day Night Band 500m Linear Lat Lon Grid Night can be accessed through the Level-1 and Atmosphere Archive & Distribution System Active Archive Center

(LADDS DAAC): https://ladsweb.modaps.eosdis.nasa.gov/missions-and-measurements/products/VNP46A1/. Additional information on the product can be found athttps://blackmarble.gsfc.nasa.gov/ and in the Black marble Users Guide located at: https://ladsweb.modaps.eosdis.nasa.gov/missions-and-measurements/viirs/VIIRS_Black_Marble_UG_v1.1_July_2020.pdf Unlimited Public downloads of Radiometrically Terrain Corrected and RGB Decompositions from the European Space Agency Sentinel-1 satellites are available from the Alaska Satellite Facility (https://asf.alaska.edu/).

REFERENCES

Alaska Satellite Facility (ASF) 2021. RGB Decomposition. Date Accessed 15 April 2021: https://github.com/ASFHyP3/hyp3-lib/blob/develop/docs/rgb_decomposition.md.

Aydin, K., T. A. Seliga, and V. Balaji, 1986: Remote Sensing of Hail with a Dual Linear Polarization Radar, Journal of Applied Meteorology and Climatology, 25(10), 1475-1484. Retrieved Jun 15, 2021, from https://journals.ametsoc.org/view/journals/apme/25/10/1520-0450_1986_025_1475_rsohwa_2_0_co_2.xml

Bang, S. D., and D. J. Cecil, 2019: Constructing a multifrequency passive microwave hail retrieval and climatology in the GPM domain. Journal of Applied Meteorology and Climatology, 58 (9), 1889-1904, doi:10.1175/JAMC-D-19-0042.1.

Bang, S. D. and D. J. Cecil, 2021: Testing Passive Microwave-based Hail Retrievals using GPM DPR Ku-band Radar. Journal of Applied Meteorology and Climatology. doi:10.1175/JAMC-D-20-0129.1.

Beeman, P., 2020: State: Derecho flattened a quarter of Iowa's forest. Des Moines Register, 20 May 2021, https://www.desmoinesregister.com/story/news/2020/11/14/state-derecho-flattened-quarter-iowas-forest/6271797002/.

Bell, J. R., and A. L. Molthan, 2016: Evaluation of approaches to identifying hail damage to crop vegetation using satellite imagery. J. Oper. Meteor., 4, 142–159, https://doi.org/10.15191/nwajom.2016.0411.

Bell, J. R., E. Gebremichael, A. L. Molthan, L.A. Schultz, F. J. Meyer, C. R. Hain, S. Shrestha, and K. C. Payne, 2020: Complementing Optical Remote Sensing with Synthetic Aperture Radar Observations of Hail Damage Swaths to Agricultural Crops in the Central United States, Journal of Applied Meteorology and Climatology, 59, 4, 665-685, https://doi.org/10.1175/JAMC-D-19-0124.1

Boryan, C., Z. Yang, R. Mueller, and M. Craig, 2011: Monitoring US agriculture: The US Department of Agriculture, National Agricultural Statistics Service, Cropland Data Layer Program. Geocarto Int., 26, 341–358, https://doi.org/10.1080/10106049.2011.562309.

Cable, J. W., J. M. Kovacs, X. Jiao, and J. Shang, 2014: Agricultural monitoring in northeastern Ontario, Canada, using multi-temporal polarimetric RADARSAT-2 data. Remote Sens., 6, 2343–2371, https://doi.org/10.3390/rs6032343.

Canisius, F., J. Shang, J. Liu, X. Huang, B. Ma, X. Jiao, X. Geng, J. M. Kovacs, and D. Walters, 2018: Tracking crop phenological development using multi-temporal polarimetric RADARSAT-2 data. Remote Sens. Environ., 210, 508–518, https://doi.org/10.1016/j.rse.2017.07.031.

Carey, L. D., M. J. Murphy, T. L. McCormick, and N. W. Demetriades, 2005: Lightning location relative to storm structure in a leading-line trailing stratiform mesoscale convective system, J. Geophys. Res., 110, doi:10.1029/2003JD004371.

Cecil, D. J., 2009: Passive microwave brightness temperatures as proxies for hailstorms. Journal of Applied Meteorology and Climatology, 48 (6), 1281-1286, doi:10.1175/2009JAMC2125.1.

Cecil, D. J., and C. B. Blankenship, 2012: Toward a global climatology of severe hailstorms as estimated by satellite passive microwave imagers. Journal of Climate, 25 (2), 687-703, doi:10.1175/JCLI-D-11-00130.1.

Cecil, D. J., 2009: Passive microwave brightness temperatures as proxies for hailstorms. Journal of Applied Meteorology and Climatology, 48 (6), 1281-1286, doi:10.1175/2009JAMC2125.1.

Cecil, D. J., and C. B. Blankenship, 2012: Toward a global climatology of severe hailstorms as estimated by satellite passive microwave imagers. Journal of Climate, 25 (2), 687-703, doi:10.1175/JCLI-D-11-00130.1.

Corfidi, S. F., M. C. Coniglio, A. E. Cohen, and C. M. Mead, 2016: A proposed revision to the definition of "derecho." Bull. Amer. Meteor. Soc., 97, 935–949, doi:10.1175/BAMS-D-14-00254.1.

Crum, T. D., and R. L. Alberty, 1993: The WSR-88D and the WSR-88D operational support facility. Bull. Amer. Meteor. Soc., 74, 1669–1687, https://doi.org/10.1175/1520-0477(1993)074<1669:TWATWO>2.0.CO;2

Depue, T. K., P. C. Kennedy, and S. A. Rutledge, 2007: Performance of the Hail Differential Reflectivity (HDR) Polarimetric Radar Hail Indicator, Journal of Applied Meteorology and Climatology, 46(8), 1290-1301. https://doi.org/10.1175/JAM2529.1.

Economic Research Service (ERS) United States Department of Agriculture, 2021: Cash receipts by commodity State ranking. Date Accessed: 5 May 2021: https://data.ers.usda.gov/reports.aspx?ID=17844#P01e86ffd75434199b5a48b8368a67860_3_251iT0R0x115.

Ferraro, R., J. Beauchamp, D. Cecil, and G. Heymseld, 2015: A prototype hail detection algorithm and hail climatology developed with the Advanced Microwave Sounding Unit (AMSU). Atmospheric Research, 163, 24-35, doi:10.1016/j.atmosres.2014.08.010.

Forkuor, G., C. Conrad, M. Thiel, T. Ullmann, and E. Zoungrana, 2014: Integration of optical and synthetic aperture radar imagery for improving crop mapping in northwestern Benin, West Africa. Remote Sens., 6, 6472–6499, https://doi.org/10.3390/rs6076472.

Freeman, A., and S. L. Durden, 1998: A three-component scattering model for polarimetric SAR data. IEEE Trans. Geosci. Remote Sens., 36, 963–973, https://doi.org/10.1109/36.673687.

Gallo, K., T. Smith, K. Jungbluth, and P. Schumacher, 2012: Hail swaths observed from satellite data and their relation to radar and surface-based observations: A case study from Iowa in 2009. Wea. Forecasting, 27, 796–802, https://doi.org/10.1175/WAF-D-11-00118.1.

Gallo, K., P. Schumacher, J. Boustead, and A. Ferguson, 2019: Validation of satellite observations of storm damage to cropland with digital photographs. Wea. Forecasting, 34, 435–446, https://doi.org/10.1175/WAF-D-18-0059.1.

Gelaro, R., W. McCarty, M. Suarez, R. Todling, A. Molod, L. Takacs, C. Randles, A. Darmenov, M. Bosilovich, and R. Reichle, 2017: The Modern-Era Retrospective Analysis for Research and Applications, Version 2 (MERRA-2), J. Climate, 30, 5419–5454, https://doi.org/10.1175/JCLI-D-16-0758.1.

Greifeneder, F., E. Khamala, D. Sendabo, W. Wagner, M. Zebisch, H. Farah, and C. Notarnicola, 2018: Detection of soil moisture anomalies based on Sentinel-1, Phys. Chem. Earth, Pt. A/B/C, 112, 75–82, https://doi.org/10.1016/j.pce.2018.11.009.

Griffin, S. M., K. M. Bedka, & C. S. Velden, 2016: A Method for Calculating the Height of Overshooting Convective Cloud Tops Using Satellite-Based IR Imager and CloudSat Cloud Profiling Radar Observations, Journal of Applied Meteorology and Climatology, 55(2), 479-491. Retrieved Jun 15, 2021, from https://journals.ametsoc.org/view/journals/apme/55/2/jamc-d-15-0170.1.xml

Haldar, D., A. Das, S. Mohan, O. Pal, R. S. Hooda, and M. Chakraborty, 2012: Assessment of L-band SAR data at different polarization combinations for crop and other landuse classification. Prog. Electromagn. Res. B, 36, 303–321, https://doi.org/10.2528/PIERB11071106.

Hogenson, K., S. A. Arko, B. Buechler, R. Hogenson, J. Herrmann, and A. Geiger, 2016: Hybrid Pluggable Processing Pipeline (HyP3): A cloud-based infrastructure for generic processing of SAR data. *2016 Fall Meeting*, Washington, DC, Amer. Geophys. Union, Abstract G32A-03

Homeyer, C. R., and K. P. Bowman, 2017: Algorithm Description Document for Version 3.1 of the Three-Dimensional Gridded NEXRAD WSR-88D Radar (GridRad) Dataset, available online at http://gridrad.org

Hosseini, M. H. R. Kerner, R. Sahajpal, E. Puricelli, Y. -H. Lu, A. F. Lawal, M. L. Humber, M. Mitkish, S. Meyer, and I. Becker-Reshef, 2020: Evaluating the Impact of the 2020 Iowa Derecho on Corn and Soybean Fields Using Synthetic Aperture Radar. Remote Sensing, 12, 3878, http://dx.doi.org/10.3390/rs12233878.

Indigo, 2020: Insights Atlas Derecho Damage, Iowa. Accessed 15 April 2021, https://www.indigoag.com/hubfs/Derecho_Report_vFINAL.pdf?hsCtaTracking=6743af10-1790-4712-8d47-ad2af4fafd70%7Ce2e218a2-bdc5-4fdb-9e0c-f2037f212ef6.

Jedlovec, G. J., U. Nair, and S. L. Haines, 2006: Detection of storm damage tracks with EOS data. Wea. Forecasting, 21, 249–267, https://doi.org/10.1175/WAF923.1.

Jiao, X., H. McNairn, J. Shang, E. Pattey, J. Liu, and C. Champagne, 2011: The sensitivity of RADARSAT-2 polarimetric SAR data to corn and soybean leaf area index. Can. J. Rem. Sens., 37, 69–81, https://doi.org/10.5589/m11-023.

Jordan, E., 2020: Cedar Rapids lost more of its tree canopy in derecho than initially estimated. The Gazette, 20 May 2021: https://www.thegazette.com/news/cedar-rapids-lost-more-of-its-tree-canopy-in-derecho-than-initially-estimated/.

Karjalainen, M., H. Kaartinen, and J. Hyyppa, 2008: Agricultural monitoring using Envisat alternating polarization SAR images. Photogramm. Eng. Remote Sensing, 74, 117–126, https://doi.org/10.14358/PERS.74.1.117.

Khlopenkov, K. V., K. M. Bedka, J. W. Cooney, and K. Itterly, 2021: Recent Advances in Detection of Overshooting Cloud Tops from Longwave Infrared Satellite Imagery. *Journal of Geophysical Research: Atmospheres*, 126, e2020JD034359. https://doi.org/10.1029/2020JD034359

Kornelsen, K.C. and P. Coulibaly, 2013: Advances in Soil Moisture Retrieval from Synthetic Aperture Radar and Hydrological Applications. Journal of Hydrology, 476, 460-489. http://dx.doi.org/10.1016/j.jhydrol.2012.10.044.

Larrañaga, A., and J. Álvarez-Mozos, 2016: On the added value of Quad-Pol data in a multi-temporal crop classification framework based on RADARSAT-2 imagery. Remote Sens., 8, 335, https://doi.org/10.3390/rs8040335.

Laviola, S., G. Monte, V. Levizzani, R. Ferraro, and J. Beauchamp, 2020: A New Method for Hail Detection from the GPM Constellation: A Prospect for a Global Hailstorm Climatology. Remote Sensing. 12. 3553. 10.3390/rs12213553.

Laviola, S., V. Levizzani, R. R. Ferraro, and J. Beauchamp, 2020: Hailstorm detection by satellite microwave radiometers. Remote Sensing, 12 (4), doi:10.3390/rs12040621.

Lee, T. E., S. D. Miller, F. J. Turk, C. Schueler, R. Julian, S. Deyo, P. Dills, and S. Wang, 2006: The NPOESS VIIRS day/night visible sensor. Bull. Amer. Meteor. Soc.,87, 191–199, doi:10.1175/BAMS-87-2-191.

Li, J., and S. Wang, 2018: Using SAR-derived vegetation descriptors in a water cloud model to improve soil moisture retrieval. Remote Sens., 10, 1370, https://doi.org/10.3390/rs10091370.

Liu, C., J. Shang, P. W. Vachon, and H. McNairn, 2013: Multiyear crop monitoring using polarimetric RADARSAT-2 data. IEEE Trans. Geosci. Remote Sens., 51, 2227–2240, https://doi.org/10.1109/TGRS.2012.2208649.

Makowski, J. A., D. R. MacGorman, M. I. Biggerstaff, and W. H. Beasley, 2013: Total Lightning Characteristics Relative to Radar and Satellite Observations of Oklahoma Mesoscale Convective Systems, Monthly Weather Review, 141(5), 1593-1611, https://journals.ametsoc.org/view/journals/mwre/141/5/mwr-d-11-00268.1.xml

McNairn, H., A. Kross, D. Lapen, R. Caves, and J. Shang, 2014: Early season monitoring of corn and soybeans with TerraSAR-X and RADARSAT-2. Int. J. Appl. Earth Obs. Geoinf., 28, 252–259, https://doi.org/10.1016/j.jag.2013.12.015.

McNairn, H., C. Champagne, J. Shang, D. Holmstrom, and G. Reichert, 2009: Integration of optical and Synthetic Aperture Radar (SAR) imagery for delivering operational annual crop inventories. ISPRS J. Photogramm. Remote Sens., 64, 434–449, https://doi.org/10.1016/j.isprsjprs.2008.07.006.

McNairn, H., Hochheim, K., and Rabe, N. 2004. Applying polarimetric radar imagery for mapping the productivity of wheat crops. Canadian Journal of Remote Sensing, Vol. 30, No. 3, pp. 517–524.

McNairn, H., van der Sanden, J.J., Brown, R.J., and Ellis, J. 2000: The potential of RADARSAT-2 for crop mapping and assessing crop condition. In Proceedings of the 2nd International Conference on Geospatial Information in Agriculture and Forestry, 10–12 Jan. 2000, Lake Buena Vista, Fla. ERIM International, Inc., Ann Arbor, Mich. Vol. 2, pp. 81–88.

McKinsey & Company, 2020: How the Iowa derecho has affected 2020 crops. Accessed 15 April 2021. https://www.mckinsey.com/industries/agriculture/our-insights/how-the-iowa-derecho-has-affected-2020-crops.

Molthan, A. L., J. E. Burks, K. M. McGrath, and F. J. LaFontaine, 2013: Multi-sensor examination of hail damage swaths for near real-time applications and assessment. J. Oper. Meteor., 1, 144–156, https://doi.org/10.15191/nwajom.2013.0113.

Molthan, A. L., J. R. Bell, T. A. Cole, and J. E. Burks, 2014: Satellite-based identification of tornado damage tracks from the 27 April 2011 severe weather outbreak. J. Oper. Meteor., 2, 191–208, https://doi.org/10.15191/nwajom.2014.0216.

Moreira, A., P. Prats-Iraola, M. Younis, G. Krieger, I. Hajnsek, and K. P. Papathanassiou, 2013: A tutorial on synthetic aperture radar. IEEEGeosci. Remote Sens.Mag., 1, 6–43, https://doi.org/10.1109/MGRS.2013.2248301.

Mroz, K., A. Battaglia, T. J. Lang, D. J. Cecil, S. Tanelli, and F. Tridon, 2017: Hail-detection algorithm for the GPM core observatory satellite sensors. Journal of Applied Meteorology and Climatology, 56 (7), 1939-1957, doi:10.1175/JAMC-D-16-0368.1.

Munich RE, 2021: Record hurricane season and major wildfires – The natural disaster figures for 2020. Accessed: 20 May 2021, https://www.munichre.com/en/company/media-relations/media-information-and-corporate-news/media-information/2021/2020-natural-disasters-balance.html.

National Aeronautics and Space Administration Earth Observatory (NASA EO), 2020: Derecho Flattens Iowa Corn. Date Accessed 15 May 2020, https://earthobservatory.nasa.gov/images/147154/derecho-flattens-iowa-corn.

National Agricultural Statistics Services (NASS), United States Department of Agriculture, 2020: personal correspondence.

National Drought Mitigation Center (NDMC), 2020: 9 August 2020 Vegetation Drought Response Index. Date Accessed 15 March 2020, https://vegdri.unl.edu/Archive.aspx.

Nighttime Microphysics RGB Quick Guide (NtMicro), 2022: Nighttime Microphysics RGB Quick Guide. Date Accessed 14 January 2022, https://www.star.nesdis.noaa.gov/goes/documents/QuickGuide_GOESR_NtMicroRGB_final.pdf.

Ni, X., C. Liu, D. J. Cecil, and Q. Zhang, 2017: On the detection of hail using satellite passive microwave radiometers and precipitation radar. Journal of Applied Meteorology and Climatology, 56 (10), 2693–2709, doi:10.1175/JAMC-D-17-0065.1.

NOAA National Centers for Environmental Information (NCEI), 2021: U.S. Billion-Dollar Weather and Climate Disasters. NOAA NECI, 20 May 2021 https://www.ncdc.noaa.gov/billions/, doi: 10.25921/stkw-7w73.

PowerOutage.US, 2021a, Electric Providers for Iowa, Accessed May 2021, https://poweroutage.us/area/state/iowa

PowerOutage.US, 2021b, Major Events, Accessed May 2021, https://poweroutage.us/about/majorevents

Przybylinski, R. W. (1995). The Bow Echo: Observations, Numerical Simulations, and Severe Weather Detection Methods, Weather and Forecasting, 10(2), 203-218. https://journals.ametsoc.org/view/journals/wefo/10/2/1520-0434_1995_010_0203_tbeons_2_0_co_2.xml

Risk Management Agency (RMA), United States Department of Agriculture, 2021: Cause of Loss Historical Data Files, Accessed March 2021, https://www.rma.usda.gov/Information-Tools/Summary-of-Business/Cause-of-Loss

Román, M.O., Z. Wang, Q. Sun, V. Kalb, S. D. Miller, A. Molthan, L. Schultz, J. Bell, E. C. Stokes, B. Pandey, K. C. Seto, and coauthors, 2018: NASA's Black Marble nighttime lights product suite. Remote Sensing of Environment 210, 113-143. https://doi:10.1016/j.rse.2018.03.017.

Rouse, J. W., R. H. Haas, J. A. Schell, and D. W. Deering, 1974: Monitoring Vegetation Systems in the Great Plains with ERTS (Earth Resources Technology Satellite). Proc. Third Earth Resources Technology Satellite Symp., Greenbelt, MD, NASA GSFC, 309–317.

Schmit, T. J., Griffith, P., Gunshor, M. M., Daniels, J. M., Goodman, S. J., & Lebair, W. J., 2017: A Closer Look at the ABI on the GOES-R Series, Bulletin of the American Meteorological Society, 98(4), 681-698, https://journals.ametsoc.org/view/journals/bams/98/4/bams-d-15-00230.1.xml.

Schultz, C. J., L. D. Carey, E. V. Schultz, and R. J. Blakeslee, 2015: Insight into the Kinematic and Microphysical Processes that Control Lightning Jumps, Weather and Forecasting, 30(6), 1591-1621. https://journals.ametsoc.org/view/journals/wefo/30/6/waf-d-14-00147_1.xml

Schwartz, M. S., 2020. "Iowa Derecho This August Was Most Costly Thunderstorm Event In Modern U.S. History" NPR. Accessed 12 July 2021. https://www.npr.org/2020/10/18/925154035/iowa-derecho-this-august-was-most-costly-thunderstorm-event-in-modern-u-s-histor.

Smull, B. F. and R. A. Houze, 1987: Rear inflow in squall lines with trailing stratiform precipitation. Mon. Wea. Rev., 115, 2869–2889, doi:10.1175/1520-0493(1987)115<2869:RIISLW>2.0.CO;2.

Steppe, J., 2020: The final 500: Last Cedar Rapids residents regaining power after derecho. The Gazette, 27 August 2020, https://www.thegazette.com/news/the-final-500-last-cedar-rapids-residents-regaining-power-after-derecho/

Spencer, R. W., M. R. Howland, and D. A. Santek, 1987: Severe storm identification with satellite microwave radiometry: An initial investigation with Nimbus-7 SMMR data. Journal of Climate and Applied Meteorology, 26 (6), 749-754.

Texas Tech University, 2004: A recommendation for an enhanced Fujita scale (EF-scale). Texas Tech University, Lubbock, TX, 95 pp. www.spc.noaa.gov/faq/tornado/ef-ttu.pdf.

Tucker, C. J., 1979: Red and photographic infrared linear combinations for monitoring vegetation. Remote Sens. Environ., 8, 127–150, https://doi.org/10.1016/0034-4257(79)90013-0.

Ulaby, F.T., and P. P. Batlivala, 1976: Optimum radar parameters for mapping soil moisture. IEEE Transactions on Geoscience and Remote Sensing, Vol. 14, pp. 81–93.

van der Walt, S., Schönberger, J. L, Nunez-Iglesias, J., Boulogne, F., Warner, J. D., Yager, N., Gouillart, E., Yu, T., and the scikit-image contributors, 2014: scikit-image: Image processing in Python. PeerJ 2:e453 https://doi.org/10.7717/peerj.453.

Vivekanandan, J., J. Turk, and V. N. Bringi, 1991: Ice Water Path Estimation and Characterization Using Passive Microwave Radiometry, Journal of Applied Meteorology and Climatology, 30(10), 1407-1421. https://journals.ametsoc.org/view/journals/apme/30/10/1520-0450_1991_030_1407_iwpeac_2_0_co_2.xml

Whelen, T.& P. Siqueira, 2018: Coefficient of variation for use in crop area classification across multiple climates. International Journal of Applied Earth Observation and Geoinformation. 67. 114-122. https://10.1016/j.jag.2017.12.014.

White, L., B. Brisco, M. Dabboor, A. Schmitt, and A. Pratt, 2015: A collection of SAR methodologies for monitoring wetlands. Remote Sens., 7, 7615–7645, https://doi.org/10.3390/rs70607615.

Wiseman, G., H. McNairn, S. Homayouni, and J. Shang, 2014: RADARSAT-2 Polarimetric SAR response to crop biomass for agricultural production monitoring. IEEE J. Sel. Top. Appl. Earth Obs. Remote Sens., 7, 4461–4471, https://doi.org/10.1109/JSTARS.2014.2322311

Yuan, M., M. Dickens-Micozzi, and M. Magsig, 2002: Analysis of tornado damage tracks from the 3 May tornado outbreak using multispectral satellite imagery. Wea. Forecasting, 17, 382–398, https://doi.org/10.1175/1520-0434(2002)017,0382:AOTDTF.2.0.CO;2.

TABLES

Table 1. Comparison of corn and soybean damage estimates for the state of Iowa. Estimates are in millions of acres.

Estimates are in millions of acres.					**USDA RMA Estimates**			
Crop	This Study	Hosseini et al. (2020)	Indigo (2020)	McKinsey and Company (2020)	Drought	Hail	Wind/Excess Wind	
Corn	1.97	1.99	2.10	2.48 - 3.42	0.59	0.03	1.01	
Soybean	1.40	0.60	1.40	0.31 – 0.76	0.33	0.02	0.07	*USDA Total*
Total	**3.37**	**2.59**	**3.50**	**3.1 – 3.8**	0.92	0.05	1.08	**2.05**

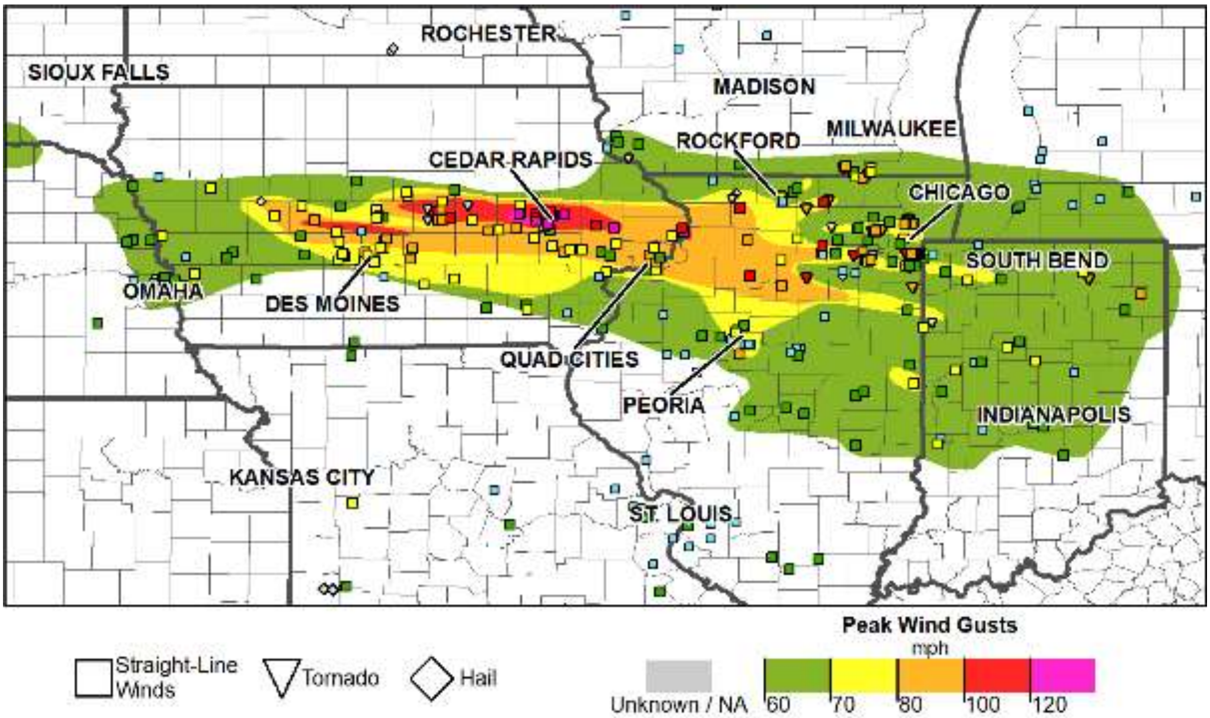

Figure 1. A map depicting severe weather reports and estimated wind swaths from the 10 August 2020 derecho. The storm reports cover the period from 1200 UTC 10 August to 0200 UTC 11 August 2020. The wind reports are a combination of the preliminary local storm reports and National Weather Service (NWS) storm surveys. Peak wind gusts are based upon NWS post-event analysis of weather station observations, damage reports, and storm surveys.

Figure 2. a) Sentinel-2 Multispectral Instrument (MSI) True color imagery from 19 August 2020 show multiple tracks created in agricultural fields from grain storage bins being rolled by the high winds. The Sentinel-2 imagery Modified Copernicus Sentinel data 2021 / Sentinel Hub. b) Flattened corn field and c) flattened soybean field after the 10 August 2020 Derecho in Iowa. Pictures are courtesy of Justin Glisan, Iowa State Climatologist, and Iowa State University. Pictures were acquired on 10 August 2020 and 11 August 2020.

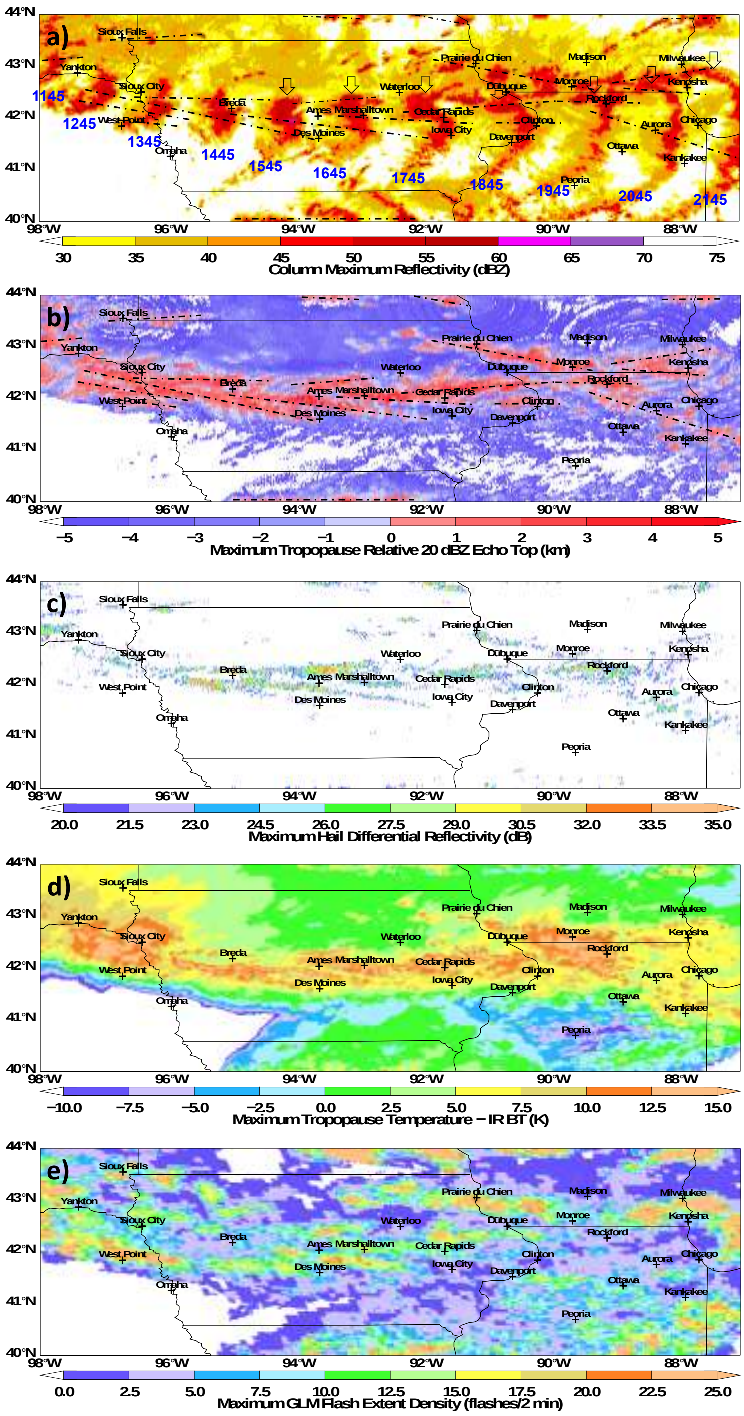

Figure 3: Composite analyses showing the most extreme values at each 2 km grid box from 1100 to 2200 UTC on 10 August 2020. a) Hourly-subsetted GridRad column-maximum Z_H b) GridRad 5-minute tropopause-relative 20 dBZ echo top height (km), c) GridRad 5-minute HDR (dBZ), d) GOES-16 1-minute ΔTrop-IR (degrees Kelvin), and e) GOES-16 GLM FED (flash detections / 2 mins). Times (in UTC) of the hourly Z_H are shown in panel a). Locations of overshooting cell tracks are identified by dashed lines in panels a-b). The comma head region within the derecho is denoted by grey arrows in panel a).

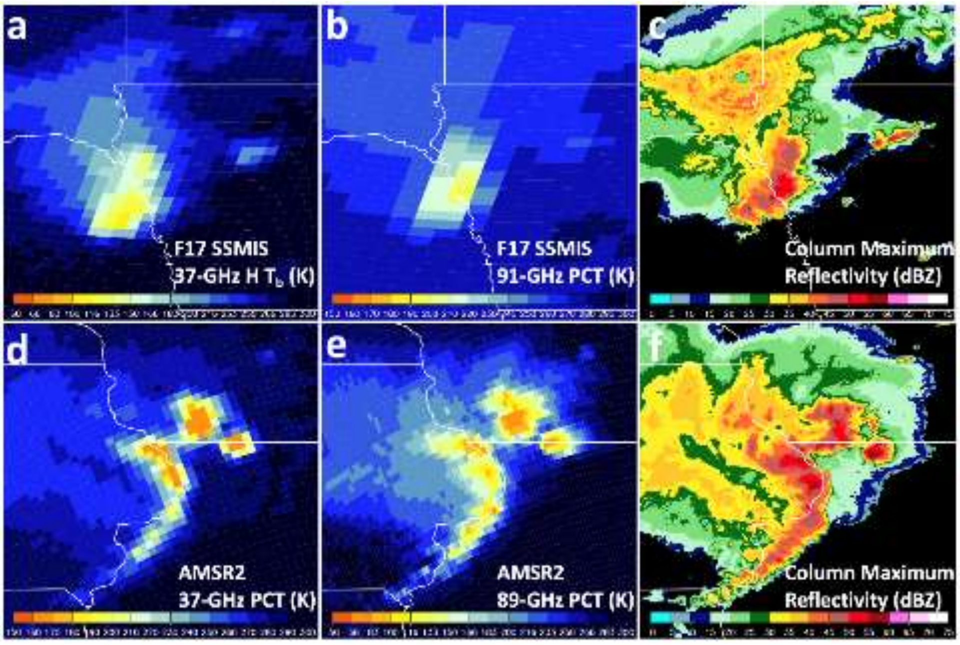

Figure 4: SSMIS passive microwave a) 37-GHz horizontal polarization channel image and b) 91 GHz polarization-corrected brightness temperature (PCT, Spencer et al. 1989) image at 1342 UTC. The SSMIS 37-GHz vertical polarization channel failed permanently in August 2016, and we therefore only present the horizontal polarization here. c) Column Max GridRad Reflectivity (dBZ) at 1340 UTC. In deep convection with significant ice scattering, the difference between the two polarizations and PCT is negligible. d-e) AMSR2 passive microwave 37 GHz and 89 GHz PCT. f) Column Max GridRad Z_H *(dBZ) at 1850 UTC*

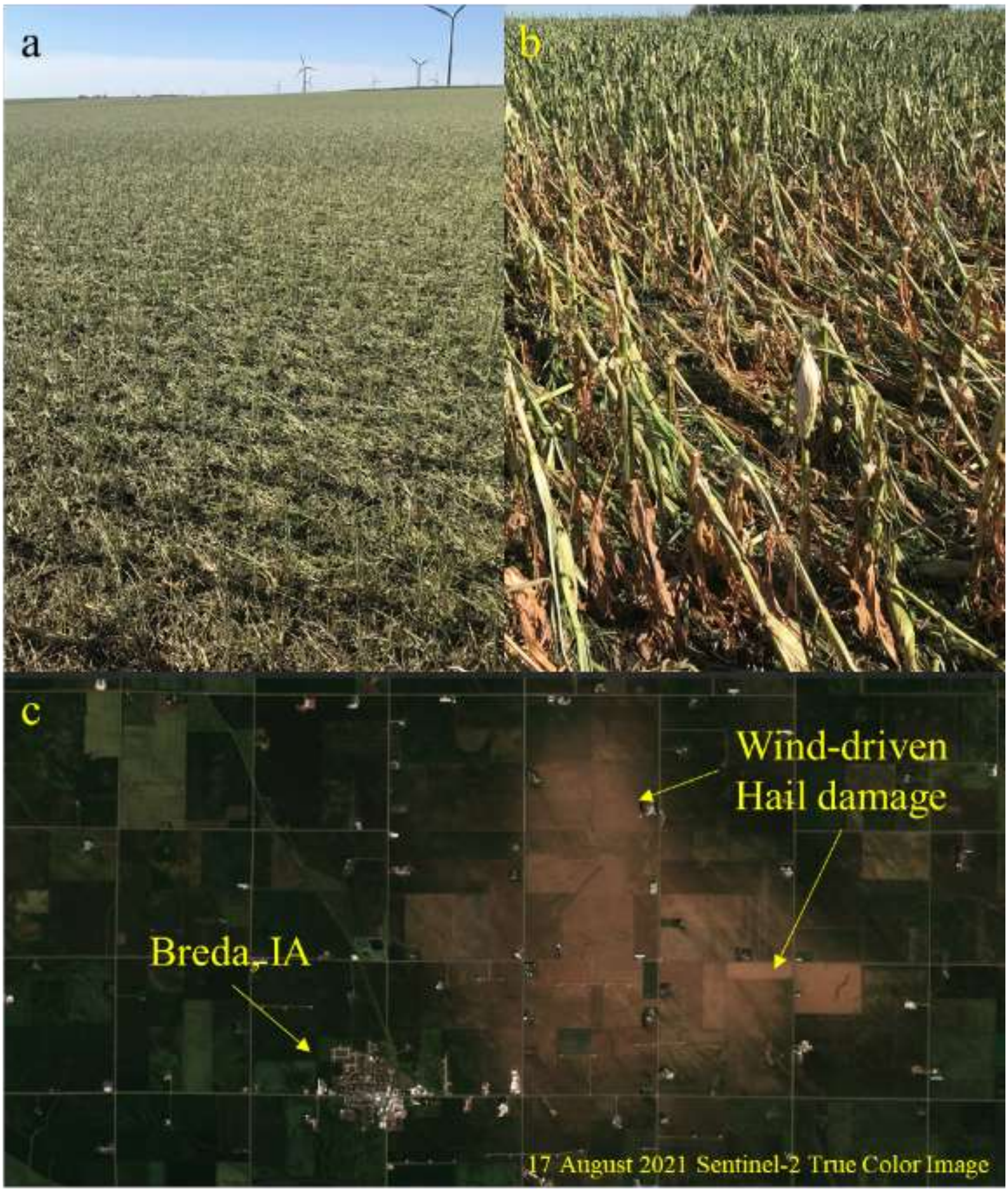

]

Figure 5. a) Soybean field damaged by wind-driven hail. b) Corn field damaged by wind-driven hail. Photos in a) and b) were both taken on 11 August 2020, courtesy of Brett Greve who provided the photos to the NOAA/National Weather Service Weather Forecast Office in Des Moines, Iowa. c) Sentinel-2 Multispectral Instrument (MSI) true color image acquired on 17 August 2020 showing an area of wind-driven hail damage (brown shades) northeast of Breda in Carroll County, Iowa. The Sentinel-2 imagery Modified Copernicus Sentinel data 2021 / Sentinel Hub.

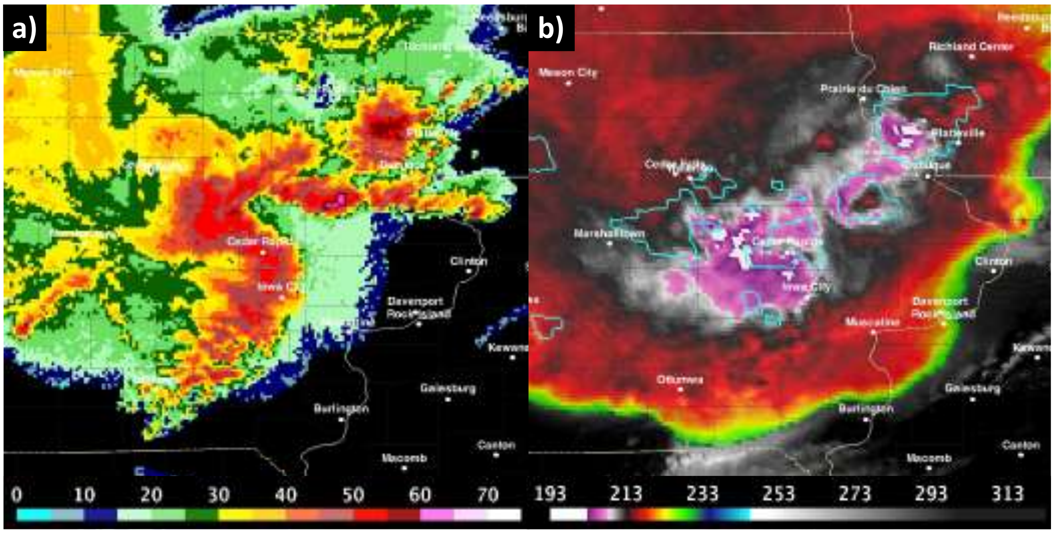

Figure 6: a) GridRad ZH at 1746 UTC as the derecho squall line was over Cedar Rapids, IA. b) Parallax-corrected GOES-16 10.3 µm visible-IR sandwich composite overlaid with FED exceeding 1 flash/minute (cyan contour)

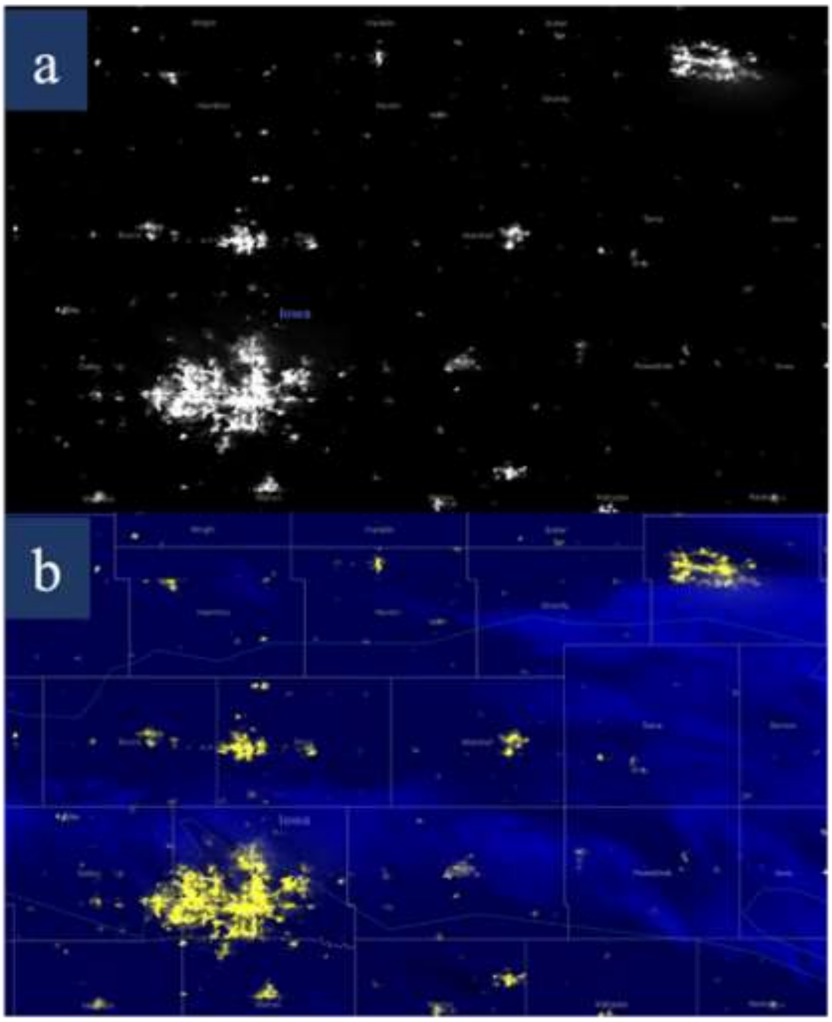

Figure 7. a) NASA Black Marble DNB imagery from 30 August 2020 over Des Moines in the southwest and Cedar Rapids in the northeast portion of the image. b) same imagery but as a false color composite which includes the longwave infrared information, allowing the cloud cover to be more easily detected on a low-moon night.

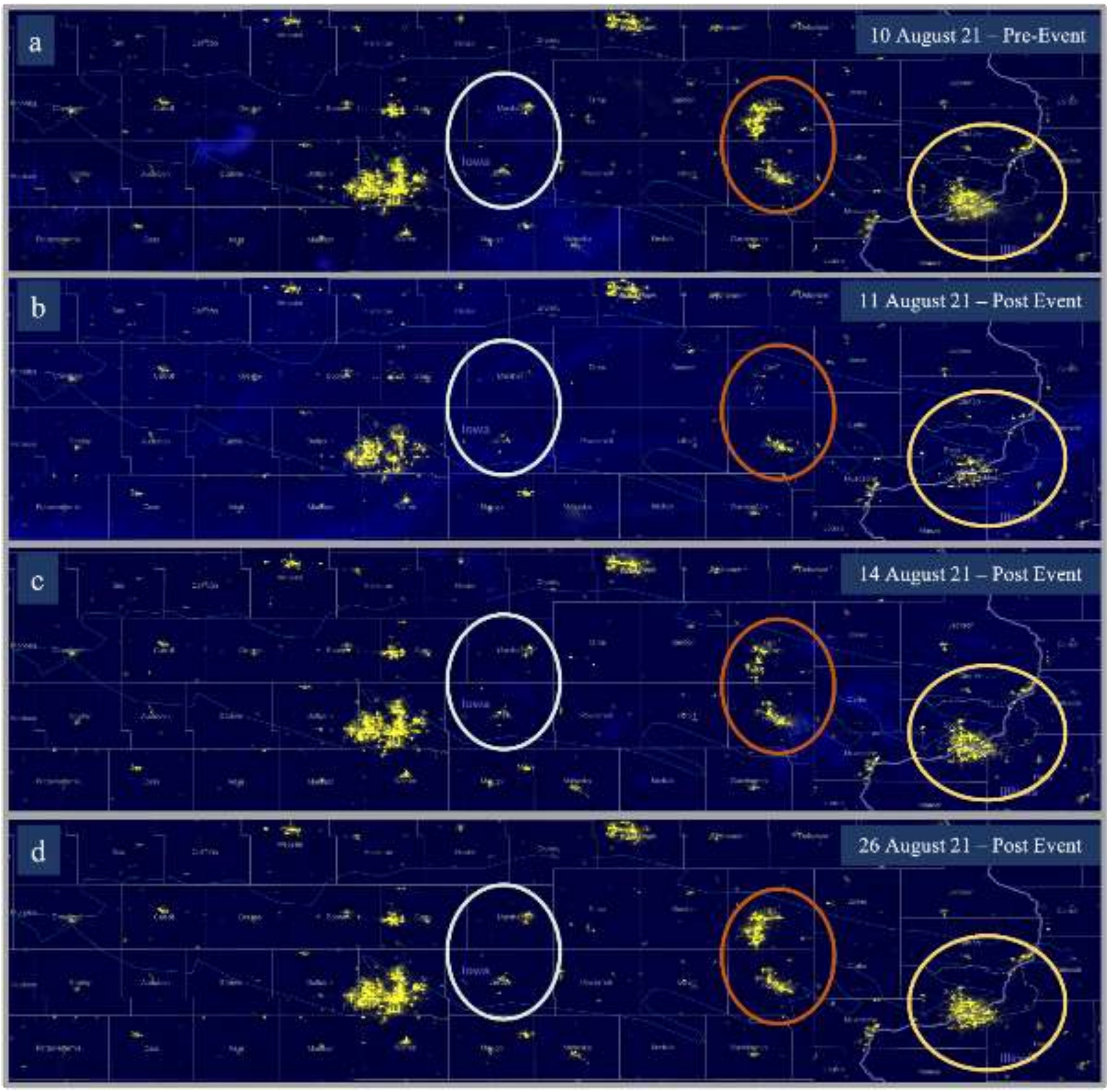

Figure 8: Time series of DNB RGB false color composites over the damaged area domain in Iowa. The image from 10 August 2020 (a) offers a pre-event approximation of what "normal" light looks like across the domain. In the image from the 11th (b), the three circled show Marshall and Jasper counties (white circle), Cedar Rapids and Iowa City (orange circle) and the Quad Cities area (yellow circle) show substantial loss of light, despite having some cloud cover that may affect the interpretation. The images from the 14th (c) and 26th (d) offer snapshots of the progress towards recovery of electric power. This information combined with reports from both power companies and government agencies provide a more complete view of the scale of the damage.

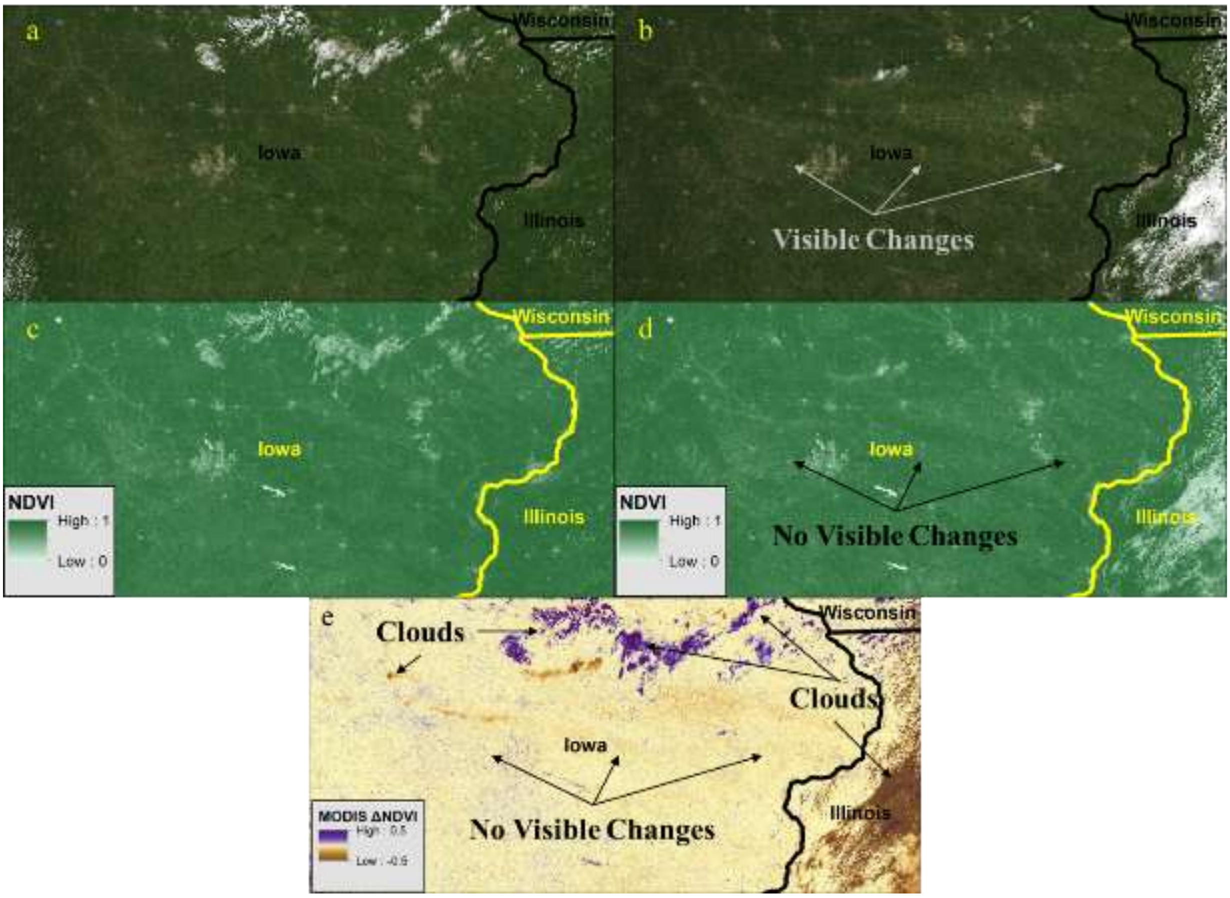

Figure 9. a) MODIS True Color Image from 28 July 2020. b) MODIS True Color image acquired on 15 August 2020. c) MODIS NDVI acquired on 28 July 2020. d) MODIS NDVI acquired on 15 August 2020. e) MODIS NDVI change between 15 August and 28 July 2020.

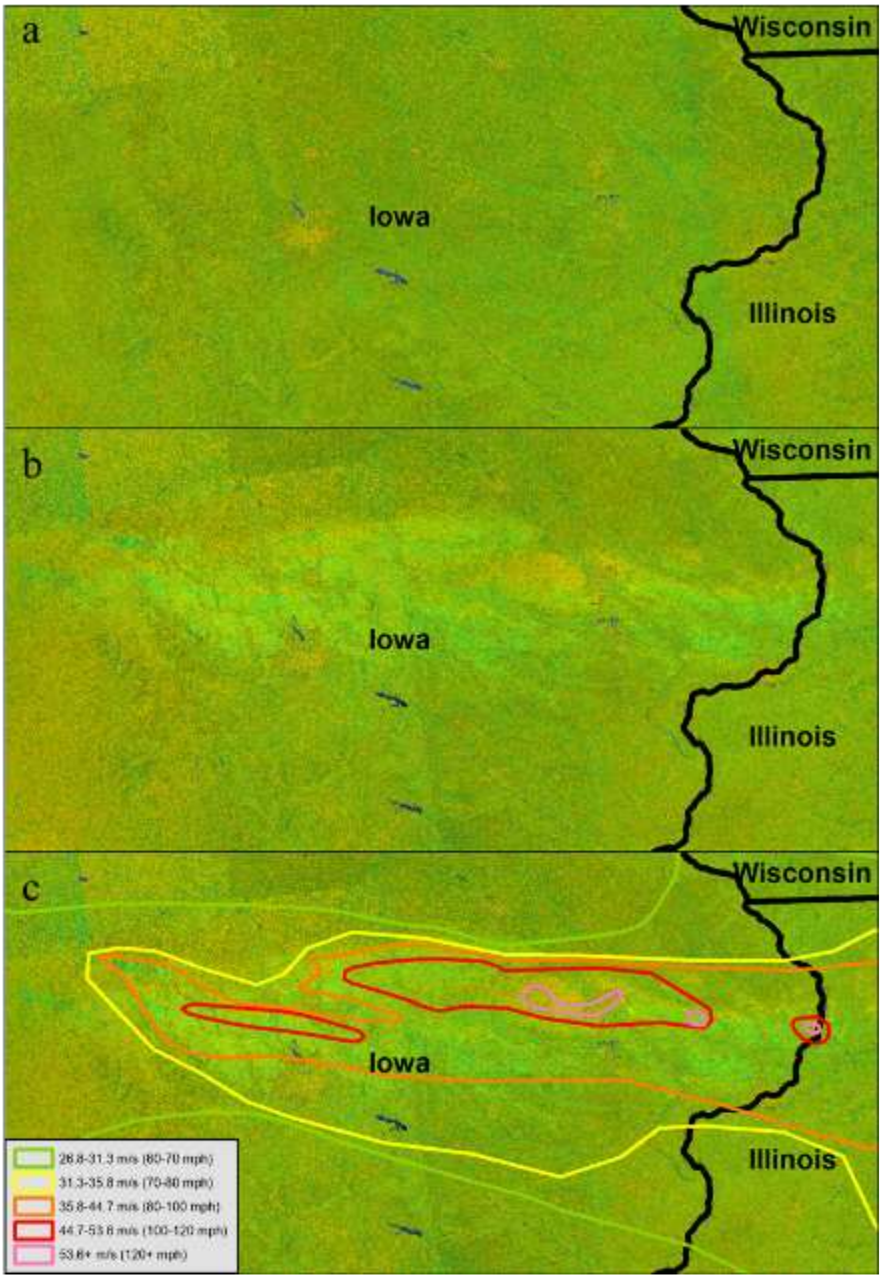

Figure 10. a) Pre-derecho Sentinel-1 RGB Decomposition composite. b) Post-derecho Sentinel-1 RGB Decomposition composite. C) Post-derecho Sentinel-1 RGB Decomposition with NWS Peak Wind Gusts overlayed.

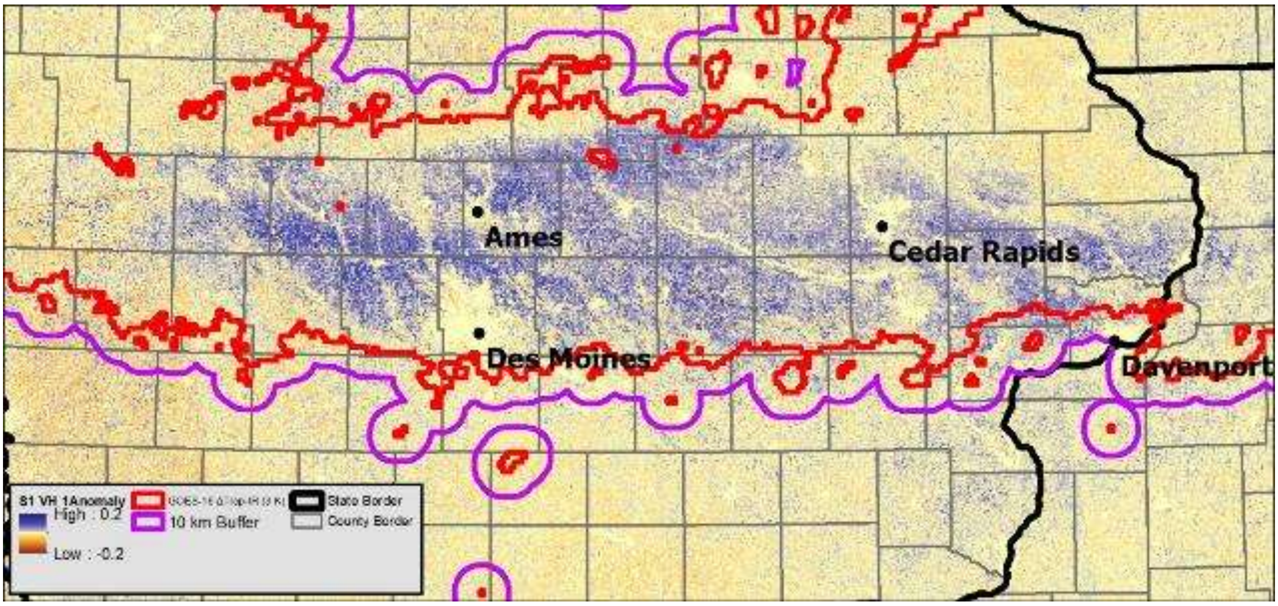

Figure 11. a) Post-derecho VH Sentinel-1 anomaly values. The anomaly values were calculated by separating the perceived "non-damaged background" and "damaged" corn and soybean pixels across Iowa and western Illinois. The perceived "non-damaged background" corn and soybean pixels were established by using the 3 K boundary of the GOES-16 ΔTrop-IR (red line) and adding a 10 km buffer (purple line). Perceived damaged pixels were to be inside the 10 km buffer.

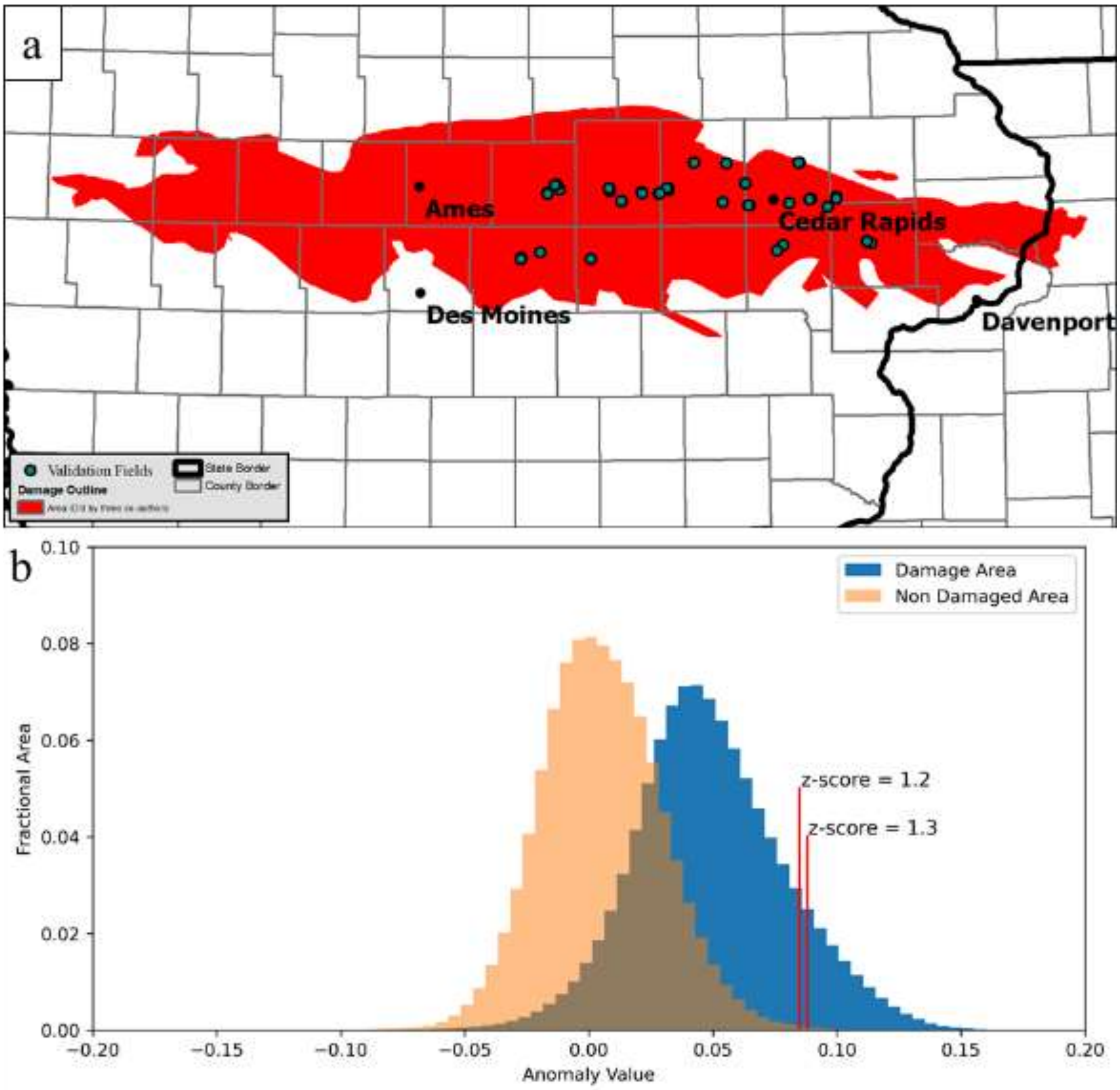

Figure 12. a) Manually derived damage extent created by three co-authors with locations of the 41 damage validation fields identified and geolocated using Civil Air Patrol (CAP) imagery. b) Histogram comparing corn and soybean pixels that were outside the damage extent and inside the damage extent c) Z-scores of corn and soybean pixels.

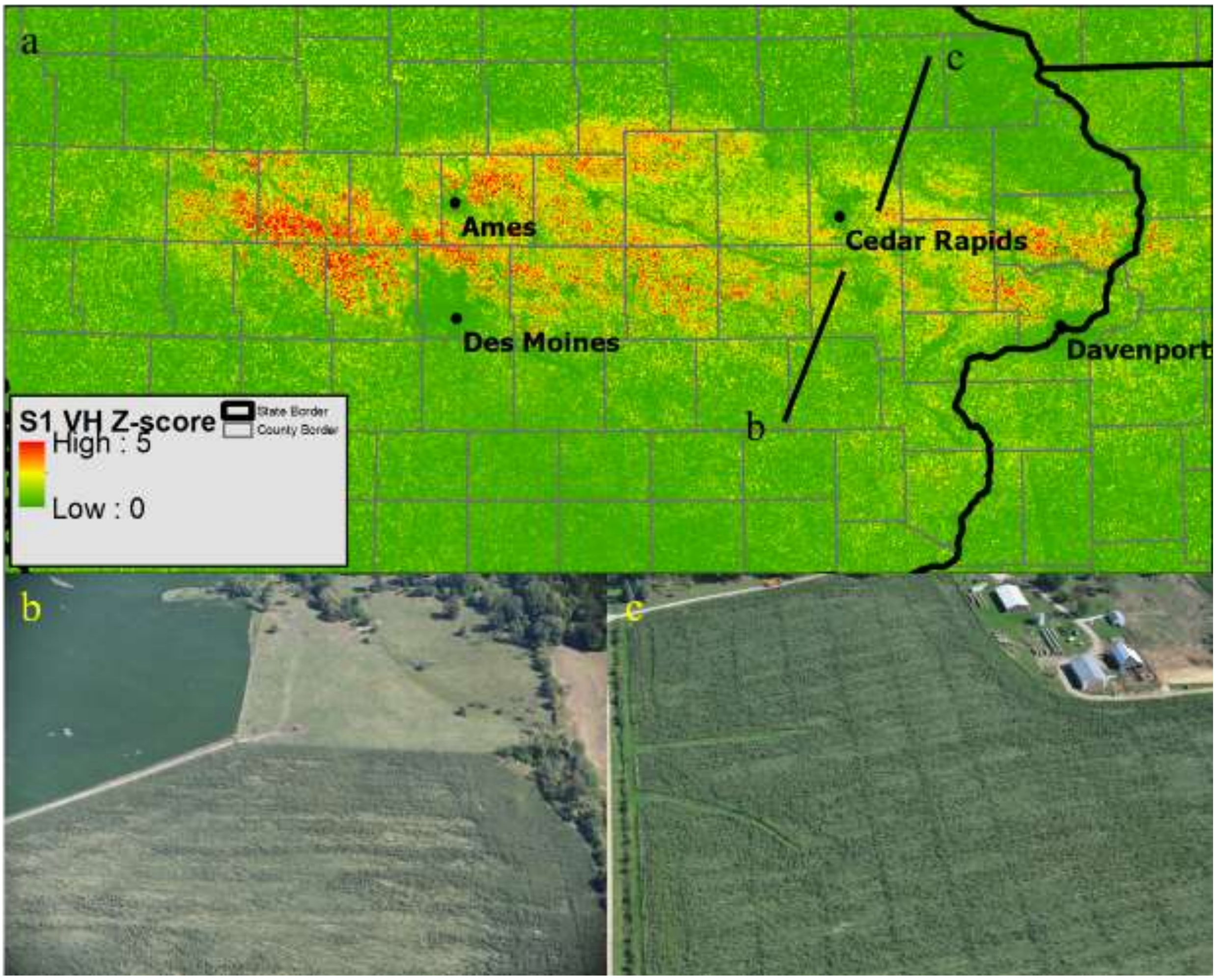

Figure 13. a) Calculated Z-scores of corn and soybean pixels b) CAP Photograph showing a flattened field in Johnson County, Iowa. c) CAP photograph showing a flattened field in Linn County, Iowa. b) and c)'s locations are denoted in a).

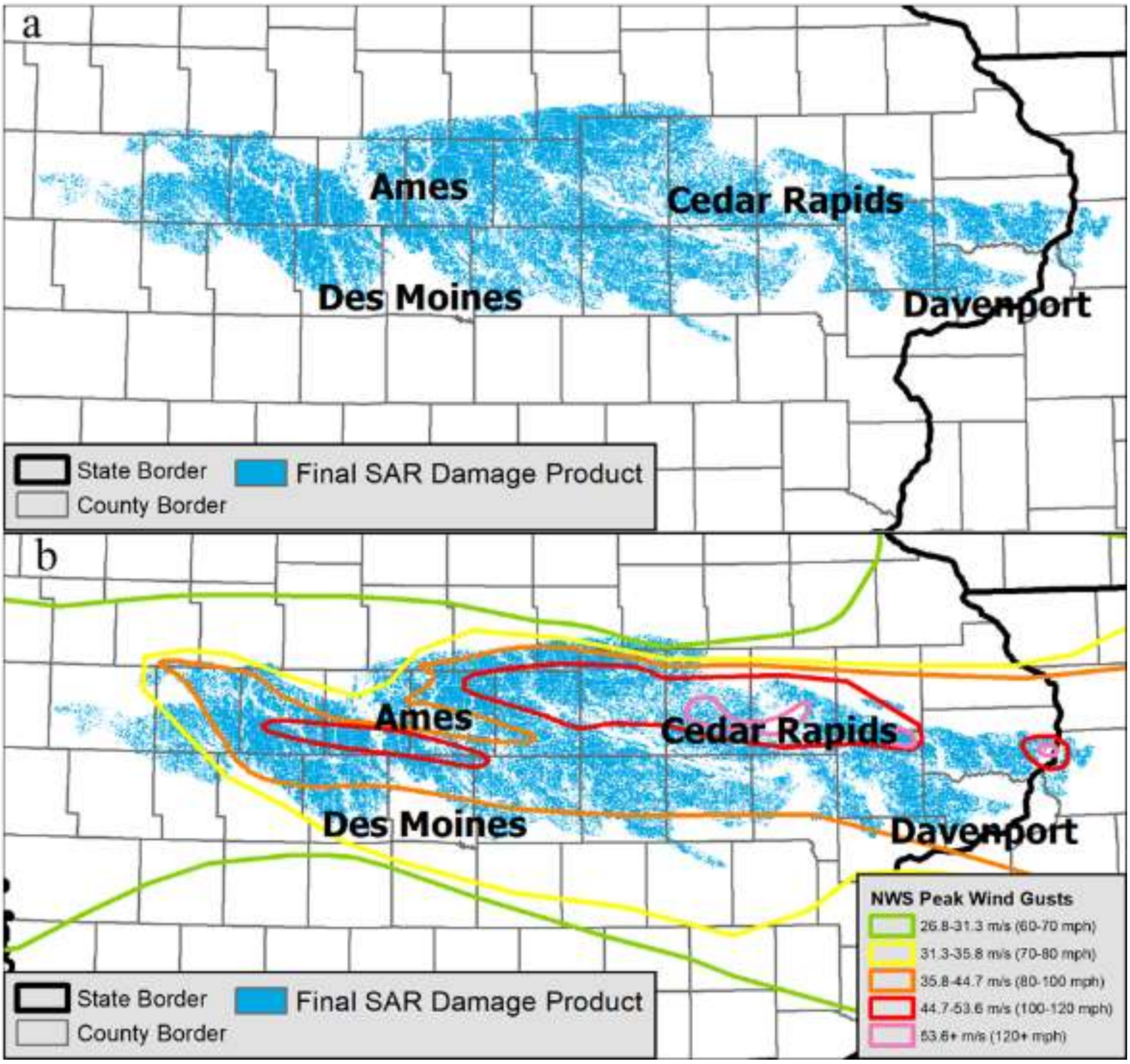

Figure 14. a) Final product using the z-score threshold of 1.25 identifying the of the corn and soybean pixels that were categorized as damaged. b) Same as a), but with the NWS peak wind gusts overlayed.

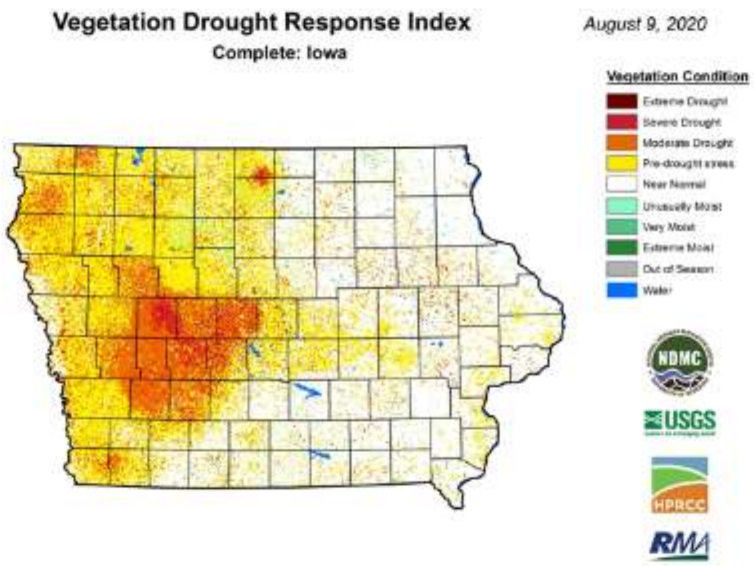

Figure 15. 9 August 2020 Vegetation Drought Response Index for the state of Iowa (NDMC 2020).